A MODIFIED SELF-INTERFERENCE BASED INCOHERENT DIGITAL HOLOGRAPHIC RECORDING SYSTEM

by

Abhinav Mishra

A thesis submitted to the faculty of
The University of North Carolina at Charlotte
in partial fulfillment of the requirements
for the degree of Master of Science in
Mechanical Engineering

Charlotte

2019

Approved by:

_____
Dr. Konstantinos Falaggis

_____
Dr. Jimmie Miller

_____
Dr. Rosario Porras-Aguilar

©2019
Abhinav Mishra
ALL RIGHTS RESERVED

ABSTRACT

ABHINAV MISHRA. A modified self-interference based incoherent digital holographic recording system. (Under the direction of DR. KONSTANTINOS FALAGGIS)

A Fresnel-type self-interference based incoherent digital holographic system that can measure the intensity and direction of incoming light field is proposed. This system is composed primarily of a convex lens as an objective, a linear polarizer, a fluorescence bandpass filter, a Geometric-Phase (GP) lens, a relay lens and a monochromatic polarized camera. The GP lens is employed as a polarization selective common path interferometer. It simultaneously modulates the incoming wavefront by its positive and negative focal lengths. The wavefront modulation and phase shifting are performed purely by the geometric phase modulation. The parallel-phase shifting method is utilized to obtain a single complex hologram by using a monochromatic polarized image sensor. With the generated hologram, it is possible to digitally reconstruct images by focusing to different planes. A modified Angular Spectrum (AS) algorithm enables an accurate and efficient wavefield propagation for reconstruction of the holograms. The system parameters for the modified Geometric Phase-Self interference Incoherent Digital Holography (GP-SIDH) architecture are analyzed and evaluated to characterize the bounds for optimum reconstruction results based on a given set of criterion.

ACKNOWLEDGEMENTS

I would first like to thank my advisor, Dr. Konstantinos Falaggis, for his unwavering support and guidance throughout my work and my time here at UNC Charlotte. This thesis would not have been possible without his passionate participation and valuable inputs at every stage of the thesis.

I would also like to thank the members of my thesis committee, Dr. Jimmie Miller and Dr. Rosario Porras-Aguilar for their continued support and their valuable comments throughout the development of this thesis. I extend my sincere gratitude to Center for Precision Metrology at UNC Charlotte for providing me access to the Metrology Lab. I acknowledge the continued support that I have received from all the faculty members and colleagues at the William States Lee College of Mechanical Engineering. I would like to also thank Dr. Ki-Hong Choi for providing valuable insights related to the GP-SIDH system architecture.

Furthermore, I would like to thank my father, Prof. Amaresh Chandra Mishra and my mother, Archana Mishra for their unequivocal support and motivation throughout the completion of this thesis, as always. Special thanks to Subhra Salki, Tulakar Jha, Anshul Karn and Shuvodeep Saha, for being a constant pillar of support by helping me overcome new challenges and inspiring me to keep working further. I would also like to extend my gratitude to all my family members and my close friends. I am profoundly grateful to everyone who made it easier for me to finish this thesis.

I have deep sense of appreciation towards Dr. Shree Bhattarai for recognizing me as a Teaching Assistant at the Department of Physics and Optical Science, which in addition to easing my financial situation, also provided me with immense inspiration to build a career in academia and research. Thank you, one and all.

TABLE OF CONTENTS

LIST OF TABLES vii

LIST OF FIGURES viii

LIST OF ABBREVIATIONS xi

CHAPTER 1: INTRODUCTION 1

1.1. Outline of thesis 5

CHAPTER 2: THEORY 6

2.1. Wave-Propagation Theory 6

2.1.1. Interference 8

2.1.2. Coherence 10

2.1.3. Polarization 11

2.2. Image formation by an optical system 13

2.3. Pancharatnam–Berry phase 15

2.3.1. Geometric-Phase Lens 16

2.4. Digital Imaging Techniques 17

2.4.1. Monochromatic Polarized Camera 17

2.4.2. High Definition Range (HDR) Imaging 18

CHAPTER 3: HOLOGRAPHIC SYSTEM ARCHITECTURES 20

3.1. System Architectures in Fresnel Holography 21

3.1.1. Fresnel incoherent correlation holography (FINCH) 22

3.1.2. Conoscopic Holography 25

3.2. FINCH based GP-SIDH system 26

3.3. Modified GP-SIDH System Architecture 28

3.3.1. Working Principle of the modified GP-SIDH system 31

3.3.2. Jones Matrix for calculating Phase-shift 32

3.3.3. Selection of Phase-Measurement Technique 33

3.4. Methodology for Reconstructing Images 35

3.4.1. Angular Spectrum Method 36

3.4.2. Formula for Reconstruction Distance 38

CHAPTER 4: SYSTEM CHARACTERIZATION 40

4.1. Experimental Setup 40

4.2. Results and Observations 43

4.2.1. Experimental Evaluation 44

4.2.2. Observations 58

CHAPTER 5: CONCLUSION 59

REFERENCES 60

LIST OF TABLES

TABLE 4.1: Distances used to quantify the parameter "Defocus" for every test run (All distances in mm). 45

TABLE 4.2: System Parameters for Experiment 2 (All distances in mm). 50

TABLE 4.3: Image reconstruction area for different f-numbers. 55

LIST OF FIGURES

FIGURE 2.1: Graphic depicting Huygens' principle for a plane and spherical wavefront. 6

FIGURE 2.2: A depiction of a wave of light. 8

FIGURE 2.3: Interference pattern of waves. The amplitudes of Wave 1 and Wave 2 add up when interfering constructively whereas they cancel each other out for the case of destructive interference. 8

FIGURE 2.4: Light waves from a point source after passing through a converging lens becomes spatially coherent. 11

FIGURE 2.5: Types of Polarization: Linear, Circular and Elliptical. 12

FIGURE 2.6: A representation of polarization states using a Poincaré Sphere. 13

FIGURE 2.7: Image Formation through a converging lens. s_1 is the object distance, s_2 is the image distance and f is the distance of principal focus from the lens. 14

FIGURE 2.8: Imaging through GP Lens. RHCP light converges where as LHCP light seems to diverge. Linearly polarized light acts as a combination of LHCP & RHCP. 16

FIGURE 2.9: Polarizer array design and a monochromatic polarized camera sensor. 18

FIGURE 2.10: An HDR frame is generated by combining images captured under varying exposure time: t_1, t_2, t_3. 19

FIGURE 3.1: General self-interference digital holographic system showing the two major phases – Hologram Recording and corresponding Image Reconstruction. 20

FIGURE 3.2: A schematic of FINCH setup. BS: beam splitter; SLM: spatial light modulator; CCD: charge-coupled device; $\Delta\lambda$ indicates a chromatic filter. 23

FIGURE 3.3: A schematic of conoscopic holography. 25

FIGURE 3.4: A schematic of GP-SIDH system by Ki-Hong Choi et. al [1]. 27

FIGURE 3.5: Setup of the modified GP-SIDH system architecture. 30

FIGURE 3.6: Illustration of parallel phase-shiting method. The structure of polarized image sensor shows that 4 pixels combine to make one complex hologram pixel [2]. 34

FIGURE 3.7: Propagation of a wave field from the source plane: g(x,y,0) to destination plane: g(x,y,z) while sampling. 36

FIGURE 3.8: System parameters schematic for finding the reconstruction distance, z_{rec}. 38

FIGURE 4.1: An image of the modified GP-SIDH system apparatus. 40

FIGURE 4.2: Top-view image of the modified GP-SIDH system apparatus. 41

FIGURE 4.3: Experimental Setup for the defocus test runs with the modified GP-SIDH system apparatus. 44

FIGURE 4.4: Test Run 1 reconstruction results for a perfectly focused interference rings pattern hologram. Image (a) depicts the absolute image of the hologram at $-z_{rec}$ and Image(b) shows the relative intensity profile for the marked section. 46

FIGURE 4.5: Reconstruction results for test run 9. Image (a) depicts the absolute image of the hologram at $-z_{rec}$ and Image(b) shows the shows the relative intensity profile for the marked section. 47

FIGURE 4.6: Reconstruction results for test run 11. Image (a) depicts the absolute image of the hologram at $-z_{rec}$ and Image(b) shows the shows the relative intensity profile for the marked section and the FWHM value of two of its peaks resembling the two points at that location. 48

FIGURE 4.7: Top View of the setup for experiment 2 with the modified GP-SIDH system apparatus. 49

FIGURE 4.8: Side View of the setup for experiment 2 with the modified GP-SIDH system apparatus. 49

FIGURE 4.9: Reconstruction results for test run 1 and the relative intensity profile for the marked section. 50

FIGURE 4.10: Reconstruction results for test run 2 and the relative intensity profile for the marked section. 50

FIGURE 4.11: Reconstruction results for test run 3 and the relative intensity profile for the marked section. 51

FIGURE 4.12: Reconstruction results for test run 4 and the relative intensity profile for the marked section. 51

FIGURE 4.13: Reconstruction results for test run 5 and the relative intensity profile for the marked section. 51

FIGURE 4.14: Reconstruction results for test run 6 and the relative intensity profile for the marked section. 52

FIGURE 4.15: Reconstruction results any without window function and the relative intensity profile for the marked section. 53

FIGURE 4.16: Reconstruction results after applying Hamming window function and the relative intensity profile for the marked section. 53

FIGURE 4.17: Reconstruction results after applying Hann window function and the relative intensity profile for the marked section. 54

FIGURE 4.18: Reconstruction results after applying Blackman window function and the relative intensity profile for the marked section. 54

FIGURE 4.19: Reconstruction results after applying Tukey window function and the relative intensity profile for the marked section. 54

FIGURE 4.20: Measuring the reconstructed image pixel area for various aperture sizes. 56

FIGURE 4.21: Apparatus setup for experiment 5 with the modified GP-SIDH system under reflective illumination. 57

FIGURE 4.22: Reconstruction results for a Socrates figurine under reflective illumination with different colormaps. 57

LIST OF ABBREVIATIONS

AS Angular Spectrum. iii, 36, 37, 39, 59

CCD Charge-Coupled Device. 23

FFT Fast Fourier Transform. 36

FWHM Full Width at Half Maximum. 47, 48, 55

GP Geometric-Phase. iii, 4, 16, 27, 39, 59

GP-SIDH Geometric Phase-Self interference Incoherent Digital Holography. iii, 4, 6, 30, 39, 59

HDR High Dynamic Range. 18, 19, 43

LC Liquid Crystal. 26

LDR Low Dynamic Range. 19

LHCP Left-Hand Circularly Polarized. 12, 32

MOS Metal-Oxide Semiconductor. 23

PSF Point Spread Function. 24

RHCP Right-Hand Circularly Polarized. 12, 32

RSD Rayleigh Sommerfeld Diffraction. 7, 35

SIDH Self-interference Incoherent Digital Holography. 3, 26, 27, 30

SLM Spatial Light Modulator. 23, 24, 27

WD Wigner Distribution. 37, 58

CHAPTER 1: INTRODUCTION

The need to communicate both, abstract and concrete ideas in an effective way, led humanity to develop visualization techniques. From the early cave paintings and the Egyptian hieroglyphs to cartography as well as Leonardo da Vinci's revolutionary methods of technical drawings for scientific purposes, all served one primary purpose – visual communication using sight. An artifact that depicts visual perception is called an image. Two primary techniques for creating an image are photography and holography.

Coined by Sir John Hershel in the year 1839, the word *Photography* owes its origin to Greek roots of *photos*, meaning light, and *graphos*, meaning writing, delineation, or painting which imparts in essence "painting with light". In the 1950s, the advent of digital photography led to significant advancements over the past decades motivated by the goal of recording a visual scene and reproducing it as close as possible to reality. However, conventional photographic recording processes use an image sensor which records only the intensity (amplitude) variations and cannot directly detect the phase of the light waves. Therefore, photographs lack the depth information of a scene encoded in the phase pattern. In order to preserve both amplitude and phase information, a different recording technique was invented. To distinguish this technique from conventional photography, it was named *Holography*. Photographs produced using the means of holography are called holograms.

The term *Hologram* was coined by Dennis Gabor who invented holography in 1947 for which he was awarded with the 1971 Nobel Prize in Physics [3]. A Greek portmanteau of *Holos* and *Gramma*, meaning, whole and something drawn, respectively. Even though only an intensity sensor is used, the phase pattern can be recorded indirectly

which carries the depth information of the object along with its intensity variation. A hologram contains the "entire message", both the amplitude and the phase information, of the incident wavefronts [3]. This phase can be detected indirectly after recording an interference pattern of the object wave with a reference wave. It is this interference pattern which is denoted as a *hologram*.

By treating light as a wave motion, coherence can be described as a measure of the degree of phase correlation that exists in the radiation field of the light source at different locations and different times. If a point source produces monochromatic light waves, its temporal coherence is perfect since the waves have a single frequency. It also has a perfect spatial coherence as there is no variation of the relative phase of the field across the optical wavefront. A high degree of light coherence is necessary for generating interference patterns. This is in contrast to the fact that most of the imaging tasks in optics are performed using natural incoherent light [4]. Various applications of holography have been limited so far since a coherent light source is required to generate an interference pattern of the incoming wavefront information.

The type of holography being focused here is incoherent digital holography. This is to create a distinction between "incoherent holography" which primarily refers to the method of recording holograms using incoherent light sources and "incoherent digital holography" which refers to recording a hologram using a digital camera and then explicitly reconstructing the hologram using digital algorithms in a computer. With the advent of powerful and smaller computers, digital holography as a whole, which is a typical example of digital imaging, has accelerated the field of indirect imaging. Although digital holography is far more complicated than direct imaging, which generally involves capturing a direct image of the scene, it has several advantages over the latter to justify its complexity. The key benefit is the ability to reconstruct a 3D image of the scene with either single, or very few camera shots.

A review study concentrating on the challenging case of interference with spatially

incoherent light reveals that research on incoherent holograms began in the mid-1960s [5, 6], where some of the pioneering systems have made use of the self-interference principle. This principle indicates that any two, or more, beams originated from the same source points are mutually coherent, and hence they can be mutually interfered. Considering the case of incoherent illumination, any two different source points are mutually incoherent. Thus, the only way to obtain any meaningful interference pattern is by using the self-interference property which then can be recorded as a hologram.

Since the 1960s, continuous development in the field of "self–interference based incoherent holography" has led to implementing several new promising systems. The holographic recording systems under the various types of incoherent light sources are reported by employing the self–referencing technique [7, 8, 9]. Such systems are widely classified under Self-interference Incoherent Digital Holography (SIDH). The wavefront modulator and phase shifter are the two key components of SIDH. First, the wavefront modulator divides the incoming spherical wave into two separate wavefronts and modulates them differently. One crucial aspect of SIDH is that the two–wave interference does not occur between the object wave that carries the object information, and the reference wave without the modulation, but between the differently modulated waves which carry the object information at the same time. There is a strong mutual coherence between wavefronts starting from the same object point at about the same time. Therefore, the interference using an incoherent light source is available. Second, the phase shifting method is introduced to eliminate the bias and twin image noises which are superposed on the complex hologram information due to the nature of the interference [10].

One primary application of incoherent digital holography is 3D imaging. Fresnel incoherent correlation holography (FINCH) is a notable invention in the field of incoherent digital holography which is also based on the self–interference principle. The

evolution of holography into many technological branches has seeded numerous different applications making use of its 3D imaging capabilities such as super-resolution imaging, spectral imaging as well as 3D fluorescence imaging and microscopy to name a few. Incoherent holography is a diverse field and there are several other methods for recording incoherent holograms such as optical scanning holography [11, 12] and mutliple view projection methods [13, 14]. These methods, however, do not make use of the self–interference property and hence, are out of the scope of the thesis.

The GP lens based SIDH system presented by Ki-Hong Choi et. al. in June 2018 served as a foundation for assembling a similar yet modified system used for the development of this thesis. In this system, the phase shifting is performed by the combination of a linear polarizer film, GP lens, and the fixed polarizer which here is a polarized camera containing a polarizer array of four different angled polarizers (90°, 45°, 135°, and 0°) placed on each pixel.

The goal was to assemble a simple optical design which would be cost-effective. The GP lens utilized in this study is a liquid crystal based flat lens with a thin form factor by using Pancharatnam–phase effect [15, 16]. The GP lens simultaneously modulates the incoming wavefront by its positive and negative focal lengths [17, 18]. Since the geometric phase modulation solely performs both the wavefront modulation and phase shifting, this system is classified under geometric phase self-interference incoherent digital holography .

A modified GP-SIDH system was assembled and various three-dimensional targets were recorded as holograms. These complex holograms were then reconstructed using MATLAB which allowed for digitally refocusing the image to a specific plane as required. The criterion for evaluation is then described which is used to study the variation of various parameters with the reconstruction quality of the image. The effects of defocus (from perfectly focused interference pattern) on the reconstruction quality is also evaluated. Furthermore, This helps us identify the bounds of the opti-

mum focused area for reconstruction of the hologram at a given f-number and object distance. Various window functions are applied and each of them are individually compared to find a best window function for eliminating parasitic signals.

1.1 Outline of thesis

This thesis is divided into three major sections.

- Section 1 comprises of Chapter 1 and Chapter 2.

  Chapter 1 introduces the topic in a broader sense and defines the scope of the work. Chapter 2 further builds on the idea by discussing some important theories, in essence, to understand the physics behind these phenomenon. This chapter is also a premise to Section 2.

- Section 2 comprises of Chapter 3.

  Chapter 3 discusses the approach for assembling the system architecture and the components needed. It also mentions the mathematical model for measuring the optical distances between the individual components which can be used for calculating the reconstruction distance with precision.

- Section 3 comprises of Chapter 4 along with the conclusion.

  Chapter 4 discusses the methodology used for apparatus setup focusing mainly on the experiments conducted to quantify the effects of varying f-number, defocus and object distances to check for improvements in reconstruction quality by comparing over a defined set of criterion. All the results obtained from the experiments are presented here. Finally, Chapter 5 provides a conclusion for the entire thesis.

CHAPTER 2: THEORY

Some fundamental concepts and technologies are revisited here to evaluate the need for choosing a specific component for the modified GP-SIDH apparatus based on which we can later characterize the system parameters.

2.1 Wave-Propagation Theory

The Dutch scientist Christiaan Huygens, in the year 1670, suggested a wave picture of light. He formulated a principle that describes wave propagation as the interference of secondary wavelets arising from point sources on the existing wavefront. More precisely, Huygens' principle when applied to light waves states that every point on a wavefront may be considered a source of secondary wavelets which spread out in forward direction at the speed of light. This can be visualized by Figure 2.1. The new wavefront is the tangential surface to all of these secondary wavelets. The wave theory of light was firmly established by Thomas Young in 1802, when he conclusively demonstrated the wave nature in his double-slit experiment.

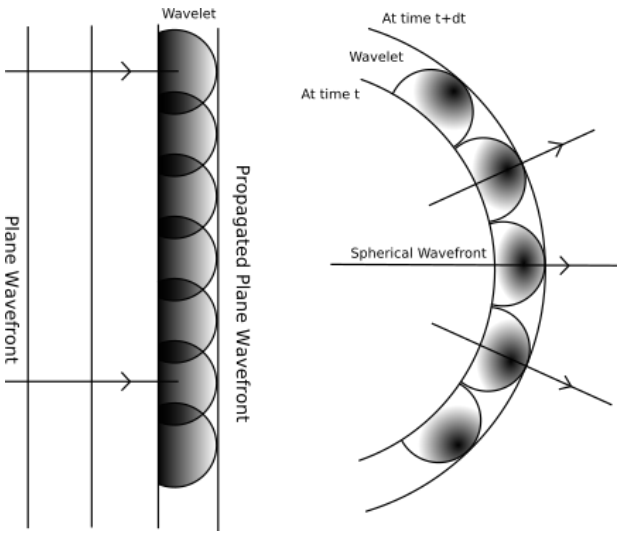

Figure 2.1: Graphic depicting Huygens' principle for a plane and spherical wavefront.

Extending Huygen's idea to include his notion of interference, French physicist Augustin-Jean Fresnel, in 1819 developed the "Huygens-Fresnel principle" after his work on the wave theory of diffraction [11]. This principle provides a basis for understanding in detail not only the classical wave propagation of light but also phenomenon such as reflection, refraction and diffraction. Based on the results of his experiments, Fresnel concluded that light waves are transverse waves and further explained the nature of light polarization.

We can mathematically express the light field of a Huygens wavelet as follows [19]:

$$U(x, y, z) = \iint_A U(\zeta,\ \eta,\ 0)\ g(x - \zeta,\ y - \eta,\ z)\, d\zeta\, d\eta \tag{2.1}$$

$U(x, y, z)$ is a expression for the light field in a linear homogeneous isotropic medium and $U(\zeta,\ \eta,\ 0)$ is the sampled $N \times N$ equidistant grids on the aperture plane which is parallel to the observation plane. Equation 2.1 is exactly the *Rayleigh Sommerfeld Diffraction (RSD)* integral formula, which can be used for both near and far fields without any approximation [19]. Wave propagation solves this integral when the impulse response given by $g(x, y, z)$ is:

$$g(x, y, z) = \frac{1/2}{\pi}\ \frac{exp(ikr)}{r}\ \frac{z}{r}\left(\frac{1}{r} - ik\right) \tag{2.2}$$

Here, $r\ = \sqrt{x^2 + y^2 + z^2}$. Thus, the convolution of $U(x, y, z)$ and $g(x, y, z)$ gives the solution for $U(x, y, z)$ as equation 2.1. Hence, propagation to any wavefield from $U(x_1, y_1, z_1)$ to $U(x_1, y_1, z_2)$ is possible for any $\Delta z = z_2 - z_1$.

In 1865, James Clerk Maxwell formulated the cohesive equations that suggested light to be an electromagnetic disturbance propagated through the field according to electromagnetic laws, which are widely known as Maxwell's equations [11]. The fields associated with electromagnetic waves are vector quantities such that, at every point in the wave, the electric field, the magnetic field and the direction of energy

propagation are mutually perpendicular. Specifying the electric field is sufficient to completely describing the electromagnetic wave as the magnetic field and corresponding Poynting vector can be determined. A graphical visualization of a wave of light is shown in Fig. 2.2. By convention, it is this direction of the electric field which is known as the polarization of the wave. The phenomena of interference, coherence and polarization are discussed below.

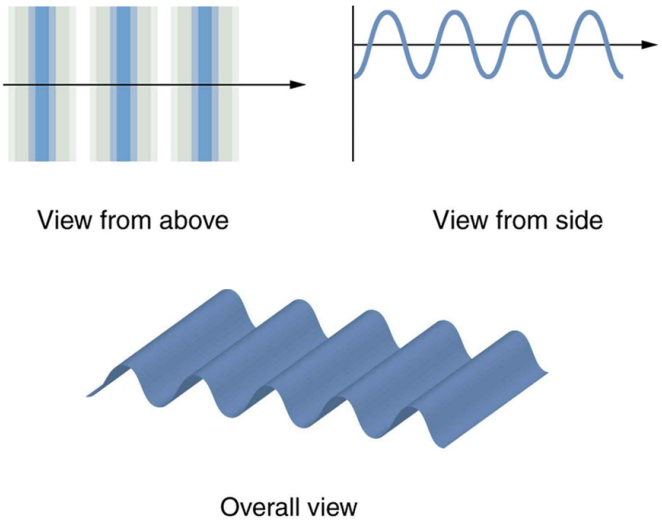

Figure 2.2: A depiction of a wave of light.

2.1.1 Interference

An interesting question that arises is *What effect of combining two waves have on their net displacement?*

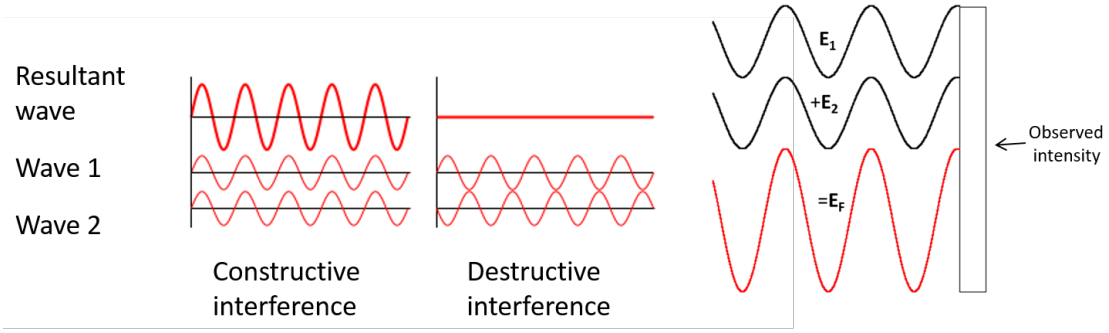

Figure 2.3: Interference pattern of waves. The amplitudes of Wave 1 and Wave 2 add up when interfering constructively whereas they cancel each other out for the case of destructive interference.

The answer lies in *superposition principle* as shown in Fig. 2.3 which states that the resultant displacement is the sum of the separate displacements of the constituent waves. The displacement of a wave is specified by its amplitude. The principle of superposition of waves states the conditions of interference which we classify as either constructive interference or destructive interference. Generally speaking, interference is a phenomenon in which two waves superimpose to form a resultant wave that can have either greater, lower, or the same amplitude. In order to observe interference of light waves, the following conditions must be met:

1. The sources of light must be coherent, that is they must maintain a constant phase with respect to each other.

2. The sources of light should be monochromatic, that is they must have a single wavelength.

Consider the interference of two plane waves of the same frequency represented by $\vec{E_1}$ and $\vec{E_2}$. These are rapidly varying electric fields with optical frequency of the order 10^{14} to 10^{15} Hz for visible light. Hence, both $\vec{E_1}$ and $\vec{E_2}$ average to zero over very short time intervals. The radiant power density, or *irradiance*, $I\,(W/m^2)$ measures the time average of the square of the wave amplitude. Hence, the interference of these waves at any plane (x, y) can be represented as:

$$I(x,y) = I_1(x,y) + I_2(x,y) + 2\sqrt{I_1(x,y)I_2(x,y)}\cos\left[\Phi_1(x,y) - \Phi_2(x,y)\right] \qquad (2.3)$$

Here the term, $\cos\left(\Phi_1(x,y) - \Phi_2(x,y)\right)$ represents the difference in phase between the two waves, with maxima occurring when the phase difference is a multiple of 2π. The term $2\sqrt{I_1(x,y)I_2(x,y)}\cos\left[\Phi_1(x,y) - \Phi_2(x,y)\right]$ is the interference term and generally denoted as I_{12}.

Since, none of the sources of light are perfectly monochromatic, for two electric fields originating from different sources, the time average of the interference phase

term equals zero. Although, the light fields from two independent sources are said to not interfere, in reality they do interfere but the interference term averages to zero over the averaging time of real world detectors. These sources are said to be mutually incoherent beams of light. On the other hand, if the light from the same source is split and recombined at the image sensor, the time average is not always zero and hence interference occurs. These light beams are mutually coherent beams. The interference pattern of fringes occur due to constructive and destructive interference.

2.1.2 Coherence

By treating light as a wave motion, coherence can be described as a measure of the degree of phase correlation that exists in the radiation field of the light source at different locations and different times. The coherence of the light wave depends on the characteristics of its source. A harmonically oscillating point source produces a perfectly coherent wave. To describe coherence for light waves, we distinguish coherence into two types:

- Temporal coherence: A measure of the correlation between the phases of a light wave at different points along the direction of propagation. Temporal coherence tells us how monochromatic a light source is. In optics, temporal coherence is measured in an interferometer such as Michaelson interferometer or Mach-Zehnder interferometer. Lasers have high monochromaticity and thus, temporally coherent.
- Spatial coherence: A measure of the uniformity of phase across the optical wavefront. An ideal point source of light has perfect spatial coherence of the wavefield since the variation of the relative phase of the field along each wavefront is zero. If a wave has only one amplitude value over an infinite length, it is perfectly spatially coherent. Coherent light can be perfect plane–waves or sphere waves. If we imagine the light to have rays, then all the rays are either parallel or radial and they never cross each other.

An incandescent bulb is an example of extremely incoherent light source. It has multiple source points which produces different wavelengths of light, making it less temporally coherent. A spectral filter can be used to increase the monochromaticity and thereby increasing the temporal coherence of the light waves. A point source produces spherical waves which after passing through a converging lens becomes spatially coherent. This is shown belown in Fig. 2.4.

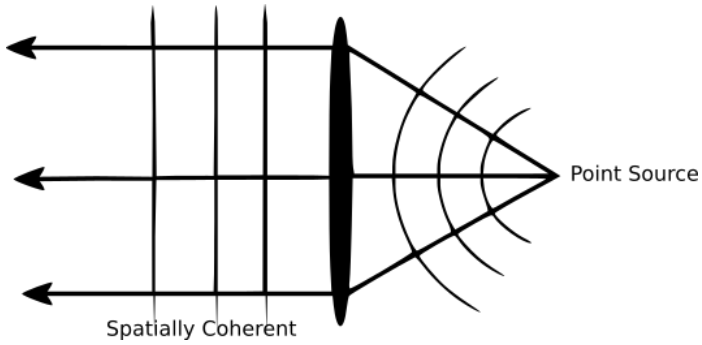

Figure 2.4: Light waves from a point source after passing through a converging lens becomes spatially coherent.

Hence, to produce a light field that is both temporally and spatially coherent, neighbouring point sources of light must produce that of the same frequency and correlated phase. A high degree of light coherence is generally needed in interferometry and holography. However, recent advances in the field of incoherent interferometry and holography has challenged this idea.

2.1.3 Polarization

The degree of polarization $P(r)$ of a quasi-monochromatic light beam at a point r is the ratio of the (averaged) intensity of the polarized portion of the beam to its total (averaged) intensity, both taken at that point. Degree of polarization and the direction of polarization are the two physical information that any polarized wave has. For a large number of optical applications, polarization is a key measurement variable and it is critical to understand its importance. The different states of polarization are described as follows:

- Elliptical Polarization: This is the most general state of polarization. When the tip of the electric field vector, $\vec{E}$, traces out an ellipse in the x-y plane. The two component might have unequal amplitudes, and also might contain a different relative phase. All the other states of polarization can be described as a special case of elliptical polarization. Some general states of polarization is shown below.
- Linear Polarization: A single transverse orientation of light wave can be considered to describe different states of polarization. Linear polarization can have either equal amplitudes or unequal amplitudes.
- Circular Polarization: If the two components of the light wave have equal amplitudes, but are not in phase with each other, and provided that there is a constant phase difference of $\frac{\pi}{2}$ between them. The tip of the electric field vector traces out a circle if we follow the wave along the z–axis at a fixed time. Hence, the name circular polarization. Circular Polarization is classified primarily as Right-Hand Circularly Polarized (RHCP) and Left-Hand Circularly Polarized (LHCP). Figure 2.5 shows different types of polarization graphically using a wave of light.

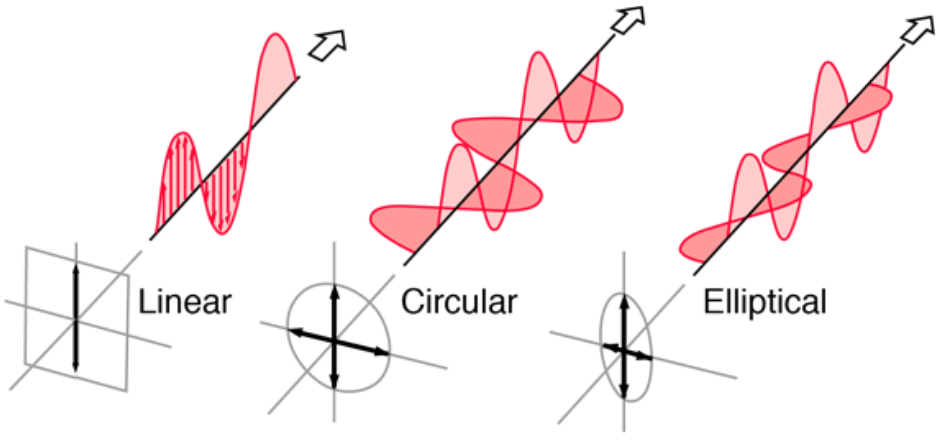

Figure 2.5: Types of Polarization: Linear, Circular and Elliptical.

The Poincaré sphere, as shown in Fig. 2.6, is a graphical tool in real, three dimen-

sional space that allows convenient description of polarized signals and of polarization transformations caused by the propagation through devices. Any state of polarization can be uniquely represented by a point on or within a unit sphere centered on a rectangular (x, y, z) coordinate system. The coordinates of the point are three normalized Stokes parameters describing the state of polarization. Partially polarized light can be considered as a combination of purely polarized light and unpolarized light intensities. The degree of polarization corresponding to a point is the distance of that point from the coordinate origin, and can vary from zero at the origin (unpolarized light) to unity at the sphere's surface (polarized light). A continuous evolution of polarization can be represented as a continuous path on the Poincaré sphere. The real, three–dimensional space of the Poincaré sphere is closely linked to the complex, two-dimensional space of Jones vector discussed in section 3.3.2.

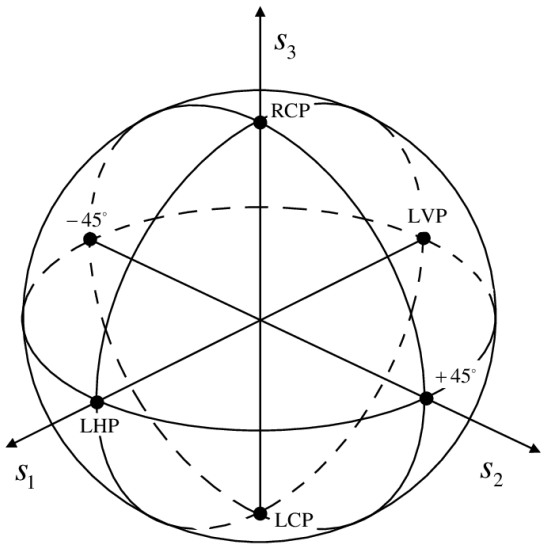

Figure 2.6: A representation of polarization states using a Poincaré Sphere.

2.2 Image formation by an optical system

Light waves spread out radially in all directions from an object. When a wavefront of light reaches a reflecting or a refracting surface in such a way that on leaving the optical surface, the wavefronts contract and the rays of light converge to a common

point. This point is defined as the image point. The object and the image point are the conjugate points for the optical system. Optical surfaces that form perfect images are called Cartesian surfaces. Optical surfaces can be either concave or convex relative to an object point.

While diverging lenses produces only virtual images, converging lens can produce both real and virtual images. The process by which images are formed at a location is the same as in mirrors. Images are formed at locations where any observer is sighting as they view the image of the object through the lens. Each observer must sight in the direction of this point in order to view the image of the object. While different observers will sight along different lines of sight, each line of sight intersects at the image location. It is useful to imagine that the rays arrive at the eye of observer viewing the image. Graphical ray tracing techniques are generally used to find the location and the nature of an image. Figure 2.7 shows a ray tracing technique.

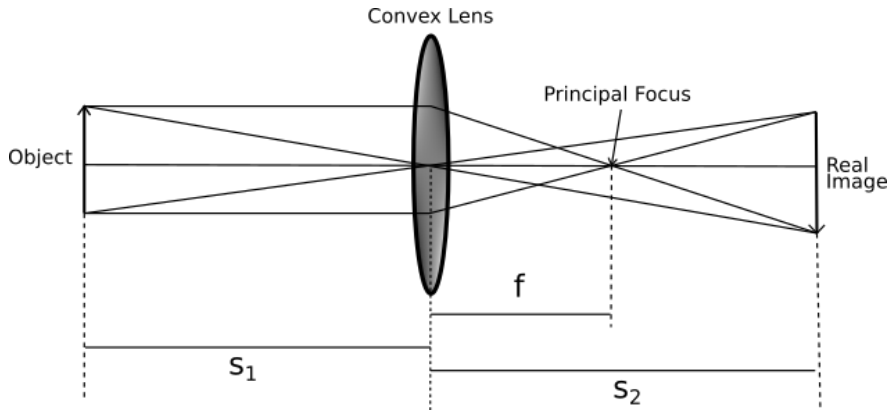

Figure 2.7: Image Formation through a converging lens. s_1 is the object distance, s_2 is the image distance and f is the distance of principal focus from the lens.

The famous *Lensmaker's equation* predicts the focal length of a lens fabricated with a given refractive index and radii of curvature. Considering the ambient medium to be air, the thin–lens equation in terms of focal length, f is given as:

$$\frac{1}{f} = \frac{1}{s_1} + \frac{1}{s_2} \tag{2.4}$$

where s_1 is the object distance and s_2 is the image distance. Figure 2.7 shows several incident rays emanating from an object - a candle. Three of these incident rays correspond to our three strategic and predictable light rays. Each incident ray will refract through the lens and be detected by a different observer. The location where the refracted rays are intersecting is the image location. The image would be real in this case since the light rays are passing through the image location. To each observer, it appears as though light is coming from this location.

2.3 Pancharatnam–Berry phase

Waves are characterized by amplitude and phase, and may vary as a function of those parameters. The geometric phase occurs when both parameters are changed simultaneously but very slowly (adiabatically), and eventually brought back to the initial configuration. Pancharatnam phase is half of the solid angle subtended by the polarization cycle on the Poincaré sphere [15].

In 1956, Pancharatnam anticipated Berry's phase [16] when he proposed how to decide if the polarization states are "in phase" [20]. To understand the physics of crystal optics, Pancharatnam's primary approach was interference of polarized light beams, geometrical approach to the polarization phenomenon, and spherical trigonometry. If the intensity of the interferogram formed by two polarized beams has maximal intensity, then these beams are said to be "in phase". This definition is analogous to that of distant parallelism in differential geometry. Polarized states can be subjected to different transformations which could be cyclic or not, adaiabatic or not, unitary or not. In all cases Pancharatnam's definition holds valid and upon further scrutiny Pancharatnam phase appears to be a generalization of Berry's phase. The relative shift of the interferogram with respect to a reference interferogram gives us the Pancharatnam phase, $\Phi_P = \delta$. By recording one interferogram after the other, once could measure their relative shift. To minimize the effects of thermal and mechanical disturbances, the intensity pattern is observed corresponding to an initial,

horizontally polarized state. This gives us the relative shift which is twice the Pancharatnam's phase [20]. The following proposition is proved by Pancharatnam [15]: the interference between mutually coherent light beams of intensities I_1 and I_2 in the polarization states P_1 and P_2 respectively is given by the expression (that defines the phase difference δ)

$$I = I_1 + I_2 + +2\sqrt{I_1 I_2}\cos P_1 P_2 \cos\delta \tag{2.5}$$

2.3.1 Geometric-Phase Lens

Polarization directed flat lenses are sensitive to circular polarization. The lenses have the unique property that one circular polarization will focus or converge through the lens (positive focal length) and the orthogonal circular polarization will defocus or diverge (negative focal length). GP Lens is a type of polarization directed flat lens which is essentially a thin (0.45mm) flat window with a complex photo-aligned liquid crystal polymer (LCP) film deposited on the surface. By varying the geometrical phase shift spatially, the LCP achieves near perfect diffraction efficiency of the holographically recorded lens wavefront. In short, a thin film equivalent of a geometric optic with very little volume, yielding significant reductions in weight and thickness.

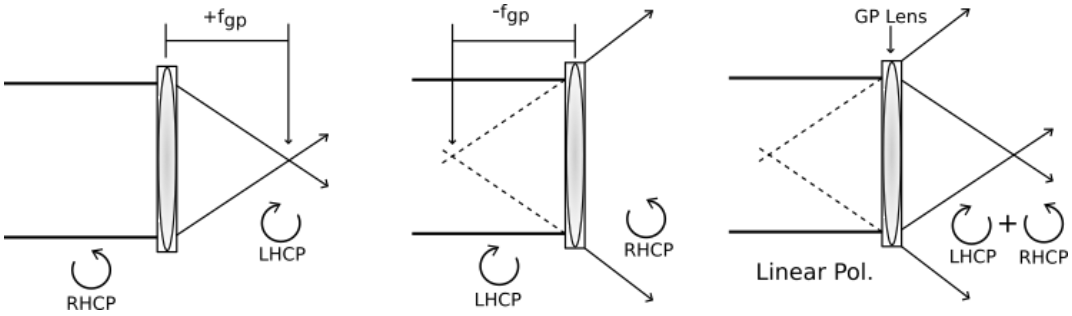

Figure 2.8: Imaging through GP Lens. RHCP light converges where as LHCP light seems to diverge. Linearly polarized light acts as a combination of LHCP & RHCP.

Fig. 2.8 shows imaging with GP Lens under different incoming light polarization. With unpolarized light, GP Lens acts as a positive lens for 50 percent of the light (one of the circular polarizations) and it will act as a negative lens for the other 50

percent of the light (orthogonal polarization). Linearly polarized light will act the same as unpolarized - 50 % of the light gets focused whereas 50 % of the light diverges with a negative focal length.

2.4 Digital Imaging Techniques

The numerical representation of a two-dimensional image by digitally encoding the visual characteristics of a scene is called digital imaging. This is primarily done to increase the accuracy of an observational data. A key advantage over analog imaging, a digital image can be used to make indefinite number of copies of the original image without any loss in quality. Furthermore, this process is far more efficient and feasible in sharing the image with as many people as possible. In all classes of digital imaging, information is converted by image sensors into digital signals that are processed by a computer which displays the output as a visible-light image on a screen. Here, we focus on a polarized camera which has several advantages over regular camera as it can capture the intensity as well as the phase of the incoming light waves. A important technique for avoiding underexposed or overexposed images is by using a High Dynamic Range (HDR) technique which is discussed in section 2.4.2.

2.4.1 Monochromatic Polarized Camera

In September 2018, Sony Semiconductor Solutions launched a polarization image sensor with four-directional polarizer which is formed on the photodiode of the image sensor chip [21]. The FLIR Blackfly® S GigE polarized camera [22] as shown in Fig. 2.9 (b) uses this sensor from Sony which provides these cameras with on-sensor polarimetry in addition to a high-speed global shutter readout. The polarization sensor has wire-grid polarizers which implies that the component of light parallel to the polarizer passes through whereas the perpendicular component is blocked. The polarizer array is comprised of four different angled polarizers (90°, 45°, 135°, and 0°) placed on each pixel. Every block of four pixels makes up a calculation unit as

shown in 2.9 (a). The relationship between the different directional polarizers in this four pixel block design as shown in Fig. 2.9, allows the calculation of both the degree and direction of polarization of the incoming light field. Polarized sensors provides on-camera processing using the four directional filters and outputs both the intensity and polarized angle of each image pixel.

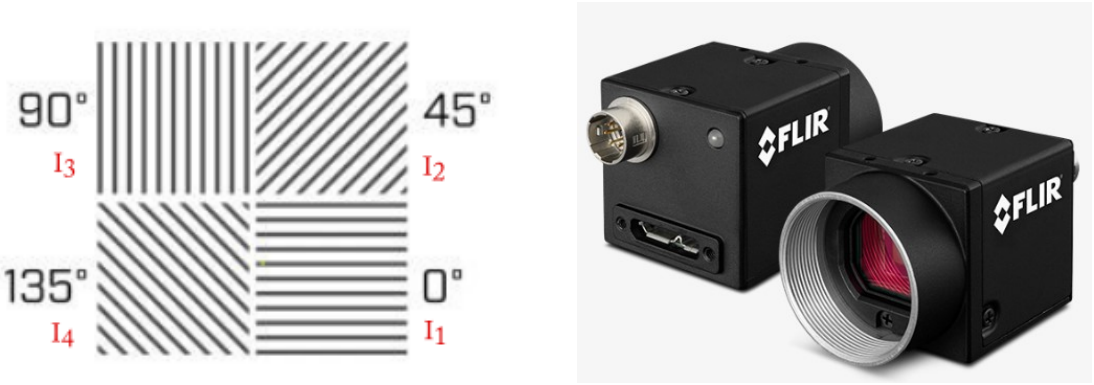

(a) 4-Pixel Block Polarizer design. (b) FLIR Blackfly® S polarized camera [22].

Figure 2.9: Polarizer array design and a monochromatic polarized camera sensor.

2.4.2 High Definition Range (HDR) Imaging

High Dynamic Range (HDR) images and video contain pixels, which can represent much greater range of colors and brightness levels than that offered by existing, standard dynamic range images. In principle, the term dynamic range is used in engineering to define the ratio between the largest and the smallest quantity under consideration. With respect to images, the observed quantity is the luminance level and there are several measures of dynamic range in use depending on the application. Each pixel value in the JPEG image encoding is represented using three 8-bit integer numbers (0-255) using the YCrCb color space which is a family of color spaces used a part of the color image pipeline in digital imaging systems. Y is the luma component, which refers to the relative brightness of the image and Cr and Cb are the blue-difference and the red-difference chroma components respectively. This color space is able to store only a small part of visible color gamut and an even smaller part of the

luminance range that can be perceived by our eyes [23]. To emphasize the limitations of traditional imaging technology is it called Low Dynamic Range (LDR) imaging. With normal LDR sensors for a mostly static scene, multiple exposures are taken in a time-sequential manner, and then merged into an HDR image using computational methods. HDR technology is immensely helpful to avoid overexposure and increase the per bit resolution of the image.

The simplest method of capturing HDR images involves taking multiple images, each at different exposure settings. While an LDR sensor might capture at once only a limited range of luminance in the scene, its operating range can encompass the full range of luminance through the change of exposure settings. Therefore, each image in a sequence is exposed in a way that a different luminance range is captured. Afterwards, the images are combined into a single HDR image by weighted averaging of pixel values across the exposures, after accounting for a camera response and normalizing by the exposure change. HDR sensors are used primarily for this reason to avoid the images being over-exposed or under-exposed.

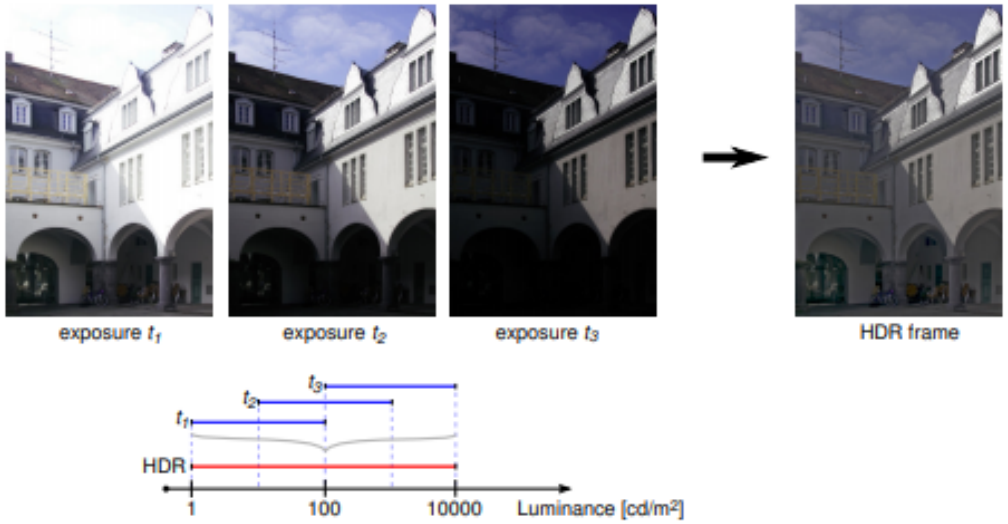

Figure 2.10: An HDR frame is generated by combining images captured under varying exposure time: t_1, t_2, t_3.

CHAPTER 3: HOLOGRAPHIC SYSTEM ARCHITECTURES

A review of various system architectures of self-interference incoherent digital holography revealed that these architectures can be generally classified into Fourier, Fresnel or generalized correlation holography. Section 3.1 focuses on Fresnel incoherent digital holography and its optical architectures. One notable type is Fresnel incoherent correlation holography (FINCH), which was proposed in 2007 by Rosen, et al. [7] as "Digital spatially incoherent Fresnel Holography". This is based on the same principle of self-interference holography. The modified GP-SIDH system architecture proposed for this thesis can be categorized as a FINCH system since the incoming wavefront is divided and modulated into two different curvatures of spherical wavefronts. This process of beam interfering demands high levels of light intensity, extreme stability of the optical setup, and a relatively narrow bandwidth light source. The general optical configuration of SIDH systems can be visualized by Figure 3.1.

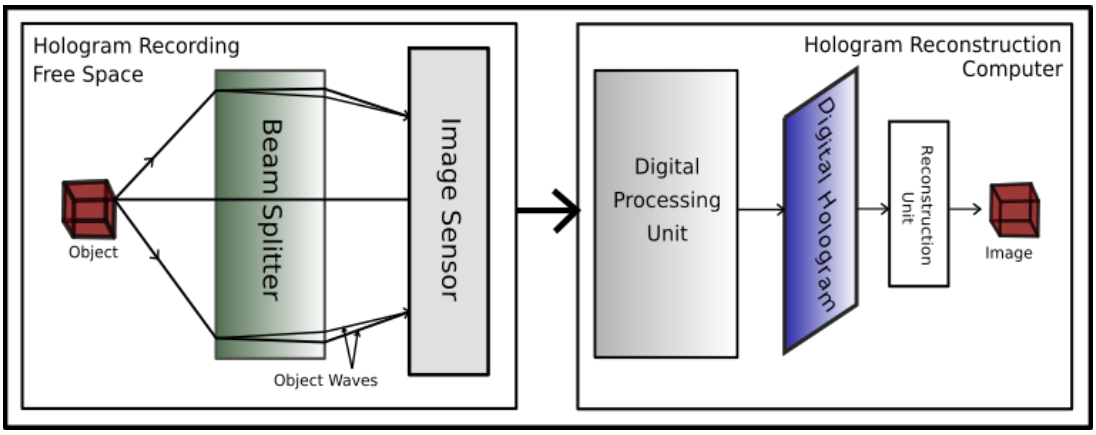

Figure 3.1: General self-interference digital holographic system showing the two major phases – Hologram Recording and corresponding Image Reconstruction.

Every object point emits light which is collected by a beam splitting system, splitting the input wave into two, but each wave is modulated differently. The two waves

are mutually coherent since they originate from the same object point and hence they can interfere on the image sensor plane. Most of the self–interference holography techniques uses this basic optical configuration. The sensor accumulates the entire interference patterns of all the object points to an incoherent hologram. One, or more of these holograms are processed by a computer and superposed into a single digital hologram. Using various reconstruction techniques, such as the angular spectrum method for propagating wave fields to different planes, the image of the object can be reconstructed along with the phase data.

3.1 System Architectures in Fresnel Holography

A Fresnel Hologram is any hologram that contains, at least, a correlation (or convolution) between an object function and a quadratic phase function. In addition to this, the quadratic phase must be parameterized according to the axial distance of the object points from the detection plane. This implies that the number of cycles per radial distance of each quadratic phase function in the correlation is dependent on the z distance of each object point. [24] Therefore, in Fresnel Holography, the overall recording process uses an optical system to generate a Fresnel hologram which is obtained as a correlation between the object and interference patterns.

In order to understand the working principle of any general Fresnel hologram, let us look at the difference between regular and Fresnel-holographic imaging system. In classical imaging systems, image formation of objects at different distances from the lens results in a sharp image at the image plane for objects at only one position from the lens. The other objects at different distances from the lens are out of focus. In FINCH system, a set of rings is projected onto the image plane for each and every point at every plane of the object being viewed. The depth of the points is encoded by the density of the rings such that the points closer to the system project denser rings than distant points. The 3D information in the volume being imaged is recorded by the recording medium, because of the encoding method. Therefore, the Fresnel

hologram facilitates reconstruction of each plane in the image space which is in focus at a different axial distance. The encoding is accomplished by the presence of a holographic system in the image path. Each holographic system has a different method to project the ring structure on the plane of the detector. An important point to note is that this graphical description of projecting rings by every object's point actually expresses the mathematical two-dimensional (2D) correlation (or convolution) between the object function and a quadratic phase function [24].

The Fresnel hologram of a point is a sum of at least three main functions, a constant bias, a quadratic phase function, and its complex conjugate. The object function is actually correlated with all three functions. However, the useful information, with which the holographic imaging is realized, is the correlation with just one of the two quadratic phase functions. The correlation with the other quadratic phase function induces the well known twin image [24].This means that the detected signal in the holographic system contains three superposed correlation functions, whereas only one of them is the required correlation between the object and the quadratic phase function. Therefore, the digital processing of the detected signal should have the ability to eliminate the two unnecessary terms. [24]

A notable invention in the field of incoherent digital holography is Fresnel incoherent correlation holography (FINCH). The first version of FINCH is a simple, compact, single-channel incoherent digital holographic system.

3.1.1 Fresnel incoherent correlation holography (FINCH)

A type of incoherent digital holography, Fresnel incoherent correlation holography (FINCH) refers to the method of producing a hologram or the resultant hologram. FINCH is based on a single channel on-axis incoherent interferometer in which the object is correlated with quadratic phase functions, but the correlation is carried out without any movement and without multiplexing the image of the scene. This method inherently does not scan the object in either space or in time. [24] Therefore,

without sacrificing the system resolution, FINCH can generate the holograms rapidly independently of the illumination. These holograms enables us to observe a complete volume in the Field of View (FOV) of the optical system.

FINCH can obtain holograms of objects illuminated by incoherent light with a common-path optical setup without an imaging lens. After the modulation with a Spatial Light Modulator (SLM), two waves have different wavefronts with different curvatures of radii and orthogonal polarizations. These waves form an incoherent hologram on the image sensor which can then be used to reconstruct the image of the object being recorded. A schematic of FINCH system is shown in Fig. 3.2 [24].

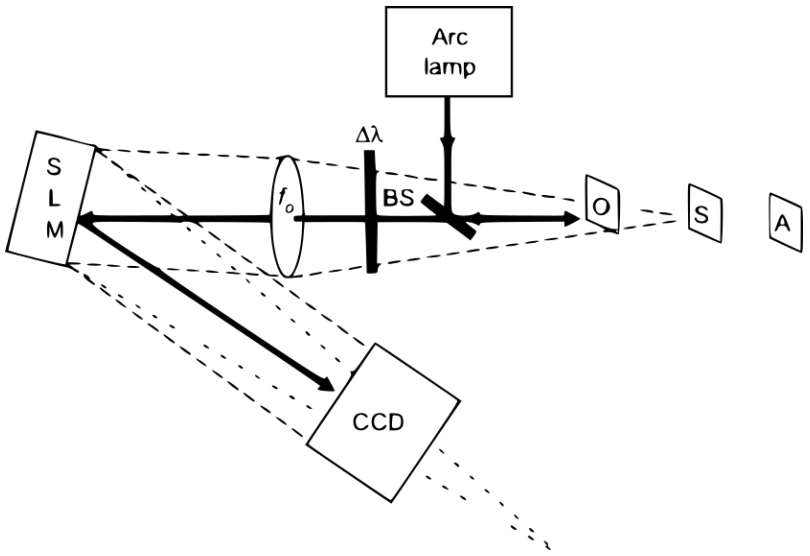

Figure 3.2: A schematic of FINCH setup. BS: beam splitter; SLM: spatial light modulator; CCD: charge-coupled device; $\Delta\lambda$ indicates a chromatic filter.

A white light source such as an arc lamp is used to illuminate the 3D scene, some of which is reflected by the objects and is captured by a Charge-Coupled Device (CCD) camera after passing through a lens L and a SLM. A CCD has Metal-Oxide Semiconductor (MOS) capacitors as its basic building block which represents a pixel. A CCD image sensor converts incoming photons into electron charges at the semiconductor-oxide interface. Usually, the analysis of such a system is carried out by following its response to an input object of a single infinitesimal point. Knowing the system's

Point Spread Function (PSF) provides crucial information about the system operation for any general object. Using Fresnel diffraction theory [25], a Fresnel hologram of a point object is obtained when the two interfering beams are, for instance, plane and spherical beams. Such a goal is achieved if the SLM reflection function $R(x, y)$ is of the form:

$$R(x,y) = \frac{1}{2} + \frac{1}{2}exp\bigg[- \frac{i\pi}{\lambda f_d}(x^2 + y^2) + i\theta \bigg] = \frac{1}{2} + \frac{1}{2}Q\bigg(- \frac{1}{f_d}\bigg)exp(i\theta) \tag{3.1}$$

where f_d is the focal length of the diffractive lens displayed on the SLM. For the sake of shortening, the quadratic phase function is designated by the function Q, such that $\mathrm{Q}(b) = \exp[(i\pi b/\lambda)(x^2+y^2)]$. When a plane wave hits the SLM, the first constant term $1/2$ in equation 3.1 represents the reflected plane wave, and the quadratic phase term is responsible for the reflected spherical wave in the paraxial approximation. The angle θ plays an important role later in the computation process to eliminate the twin image and bias term. In the present case, the Fresnel hologram generated is digital and the reconstruction is done by the computer. A phase shifting procedure of on-axis digital holography is applied to remain with a single correlation term out of three terms. Three digital holograms of the same object are recorded each with a different value of phase constant θ. The final hologram H_F is a superposition according to the following equation:

$$\begin{aligned} H_F(x,y) = {} & H_1(x,y)[exp(\pm i\theta_3) - exp(\pm i\theta_2)] \\ & + H_2(x,y)[exp(\pm i\theta_1) - exp(\pm i\theta_3)] \\ & + H_3(x,y)[exp(\pm i\theta_2) - exp(\pm i\theta_1)] \end{aligned} \tag{3.2}$$

where $H_i(x, y)$ is the i-th recorded hologram and θ_i is the phase constant of the i-th SLM's quadratic phase used during the recording process. The choice between the signs in the exponents of Eq.(3.2) determines which image, virtual or real, is kept

in the final hologram. A 3D image $g'(x, y, z)$ can be reconstructed from $H_F(x, y)$ by calculating the Fresnel propagation formula as follows:

$$g'(x, y, z) = H_F(x, y) * exp\left[\frac{\pm i\pi}{\lambda z_r}(x^2 + y^2)\right] \tag{3.3}$$

Using a computer, the hologram $H_F(x, y)$ was reconstructed by calculating the Fresnel propagation towards various z propagation distances according to Eq.(3.3). This provides a holographic reconstruction of an object with volume by moving across different planes of focus.

3.1.2 Conoscopic Holography

Conoscopic holography is a type of Fresnel Holography which has a similar optical architecture as the modified GP-SIDH system. Conoscopic holographic system facilitates recording holograms with incoherent or partially incoherent light. This technique enables the development of compact on-axis digital holography. The optical configuration for such a system is shown in figure 3.3.

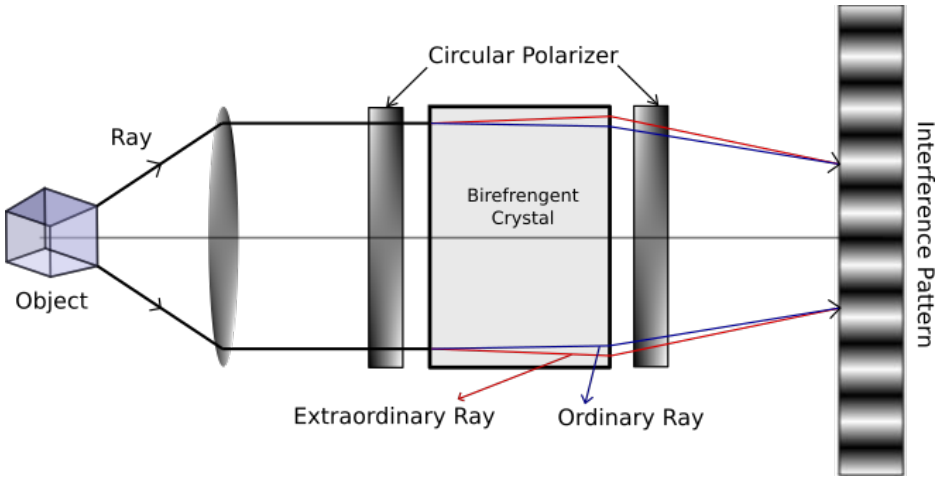

Figure 3.3: A schematic of conoscopic holography.

Light from a self-luminous object passes through a polarizer. This polarized light splits into two beams with orthogonal linear polarizations upon reaching the birefringent crystal. These two light waves with different polarization orientations passes

through a second polarizer to create interference between them. In general, the birefringent crystal generates two waves of light which originates from the same object point and these waves propagate through different refractive indices. The image sensor receives the two wavefront with different spherical curvatures which generates a hologram as these wavefronts are mutually coherent. Using this hologram, any object point can be reconstructed at its original location in 3D-space. The birefringent crystal is similar to the Geometric Phase (GP) lens, used for the modified GP-SIDH system, as they serve as a common-path wavefront modulator inside the incoherent holographic system. This system, based on FINCH with a birefringent crystal has already proven its extreme capability in the field of holographic microscopy [26]. However, it requires a variable waveplate or the combination of the waveplates to obtain a phase-shifted digital hologram. On the other hand, the GP-SIDH system uses a GP-lens instead of birefringent crystal. The GP Lens is originally designed as a half-waveplate, the geometric phase-shifting method with the rotation of the linear polarizer is effectively applied, bringing a overall simplicity in the system design.

3.2 FINCH based GP-SIDH system

Development of a compact incoherent holographic camera is essential for practical usage across all fields. By employing the self-referencing technique [7], many holographic systems have been reported. Such systems are widely classified as a self-interference incoherent digital holography (SIDH). A wavefront modulator, dividing the incoming spherical wavefront into two, which is then modulated differently, and a phase shifter are two key components of SIDH. The phase shifting method is introduced to eliminate the bias and twin image noises which are superposed on the complex hologram information due to the nature of interference [10]. Moving optical components in sub-wavelength units, or adjusting the optical path using retardation is used widely as a phase shifting technique. Piezo-actuators and Liquid Crystal (LC) plates are the most common devices to shift the phase. The phase-only SLM

is utilized as a common-path interferometer as well as the phase shifter in FINCH holographic system as discussed in Section 3.1.1. Instead of using an SLM as employed in FINCH, a birefringent crystal lens, or transmissive LC gradient index lens, is utilized for SIDH systems, which functions the same as the diffractive lens used in the FINCH system. The inherent drawbacks of SLM, such as high demanding performance or device characteristics to express the lens pattern accurately, along with high diffraction efficiency can be resolved by using passive type optical components, such as birefringent crystal or a GP hologram lens [27]. The GP lens converges or diverges the incoming circularly polarized light according to its direction of rotation. For unpolarized or linearly polarized light, the GP lens produces real and virtual images at the same time. Unlike FINCH, SIDH systems using conventional interferometer structures only require low-cost optics increasing its accessibility for research.

A relatively simplified Fresnel-type self-interference incoherent digital holographic recording system is proposed by *Ki-Hong Choi et.al* [1].

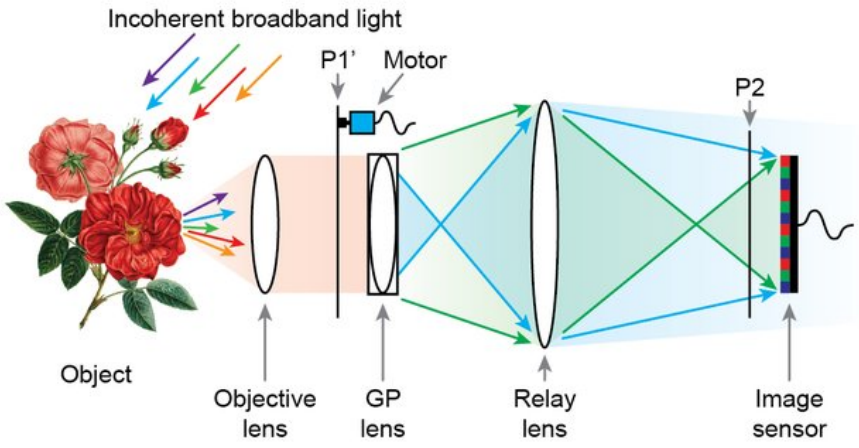

Figure 3.4: A schematic of GP-SIDH system by Ki-Hong Choi et. al [1].

The main part of the system consists of the two linear polarizers and geometric phase lens. The geometric phase lens is employed as a polarization-sensitive wavefront modulator and a single path beam splitter. This special optics has several features, such as high transparency, a modulation efficiency up to 99%, few millimeters thin,

and a flat structure. One of the polarizers is rotated by the motor and serves as a phase-shifter with the geometric phase lens, to eliminate the bias and twin image noise. A schematic of GP-SIDH is shown in Figure 3.4. The focal length of 100 mm convex lens is used as an objective lens. Before the GP lens, the linear polarizer film is located. This polarizer is attached and rotated by the micro servo-motor which is controlled by the Arduino Uno board. The GP lens is placed behind the objective lens. Both diverging and converging beams are collected and relayed by a 50 mm f/1.4 manual focus lens. The lens is located after the GP lens with reversed configuration. This lens is employed to make the interference fringe radius as large as possible on the image sensor plane, but also to maintain the optical path length as short as possible in current condition. The fixed linear polarizer and image sensor are located in order. Using the four-step phase shifting method, holographic recording under incoherent light source is available. Furthermore, using numerical reconstruction techniques and eliminating the bias and twin image, the holographic acquisition and re-focusing capability of this system is successfully demonstrated.

3.3 Modified GP-SIDH System Architecture

The three major disadvantages of traditional holographic recording systems are:

1. System size is bulky because they have a cumbersome interferometer structure or opto-electronic devices.

2. Generally, a coherent light source, such as a laser is required to record the interference patterns correctly which makes it difficult for use in daily life.

3. Hologram video recording is hard to achieve because a time-division phase-shifting technique is performed to solve the bias and twin image problems for the case of on-axis holography.

Overcoming these drawbacks provides great opportunity for realizing a compact

holographic video recording system capable of operating under various types of incoherent light sources. In a recent work by *Ki-Hong Choi et.al.* [2], a video-recording capable compact incoherent digital holographic system is proposed. Unlike their earlier architecture, this system consists of linear polarizer, convex lens, geometric phase lens, and a polarized image sensor. The second polarizer from the previous architecture has been replaced by a polarized camera containing the micro-polarizer array which is attached onto the pixel array. Also, the relay lens has been eliminated in this architecture which was earlier used to reduce the difference in curvature of the two wavefronts. By fabricating a custom-made GP lens with longer focal length and by placing the sensor closer to the GP lens, these issues have been addressed for this compact GP-SIDH system. However, for the architecture assembled for this thesis, a relay lens was included in the system. The motive behind this was to characterize two parameters and their relationship with the reconstruction quality of the holograms based on a defined set of criterion discussed in detail below. These parameters are *Defocus* and *Aperture Size*, both of which can be modulated by a relay lens.

The interference due to superposition of the two wavefronts can occur only when the optical path length difference (ΔOPL) at a certain sensor location is shorter than the coherence length c_l, given by $c_l = \lambda^2/\Delta\lambda$, where λ is the central wavelength and $\Delta\lambda$ is the spectral bandwidth of the light source [1]. In the short focal length of GP lens, the curvature differences between the two converging and diverging waves after the GP lens is too large, such that only a small overlapping area fulfills the condition of $\Delta OPL \leq c_l$. Therefore, including a relay lens for the modified GP-SIDH architecture allows us to reduce the difference in curvature of the two wavefronts and also enables us to characterize the system parameters for the architecture proposed here.

For the case of single-exposure bias and twin image elimination, either the off-axis system configuration [28], or parallel phase shifting method is applied for the

SIDH systems [29]. Both of these methods sacrifice the spatial resolution instead of losing the temporal resolution, however, the off-axis method is less desirable since the limitation of the narrow bandwidth of the image sensor [30]. On the other hand, the parallel phase-shifting method requires four adjacent pixels to record a single complex-valued data, therefore the pixel array of $M \times N$ is reduced by half to $\frac{M}{2} \times \frac{N}{2}$ [31]. Since this method employs geometric phase-shifting using a combination of waveplates and polarizers, and their relative angle, the parallel phase-shifting method is chosen as it simplifies the system architecture to some extent [27].

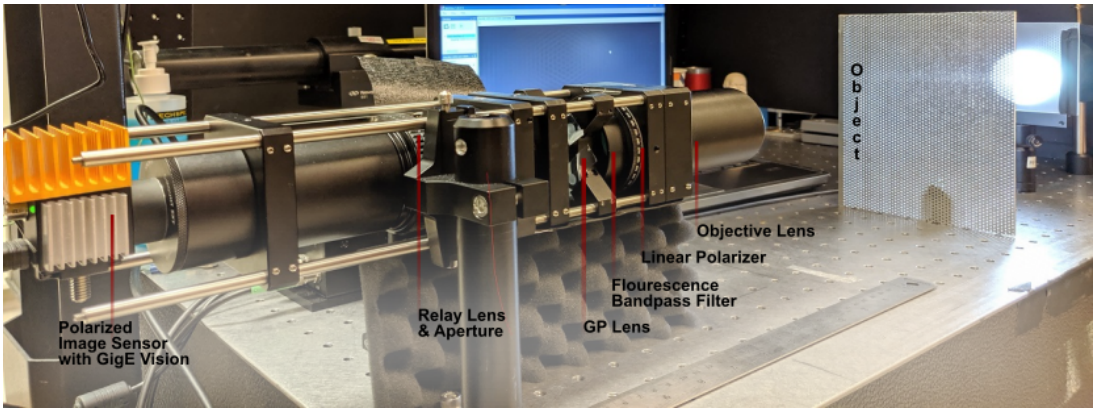

Figure 3.5: Setup of the modified GP-SIDH system architecture.

The modified GP-SIDH setup is shown in Fig. 3.5. Moving from right to left, first a 100 mm convex lens, O is placed as an objective which collects the incoming spherical wavefront ensembles of light and converges to make it spatially coherent. Then, immediately after the lens is the linear polarizer, P. After the polarizer P, a fluorescence bandpass filter with a center wavelength of 520 nm and a transmission efficiency of 93% is placed just before the GP lens to overcome the wavelength dependency on the focal length of GP lens. The GP Lens placed after the bandpass filter acts as polarization selective common path interferometer. Since, the light passing through the polarizer is linearly polarized, which can be considered to be a superposition of two orthogonal circularly polarized components. This light after passing through the GP lens, is simultaneously divided into both converging and diverging waves. The 50

mm f/1.4 relay lens is placed next in reversed configuration to focus the interference fringes on the image sensor of a polarized camera. This camera consists a polarizer array with four different angled polarizers (90°, 45°, 135°, and 0°) placed on each pixel. A four-step phase shifting method is carried out by the combination of the linear polarizer, GP lens, and the polarized image sensor.

3.3.1 Working Principle of the modified GP-SIDH system

By referring to the expressions of the FINCH system as discussed in section 3.1.1, the modified GP-SIDH system is described. The wave field of light emitted by each point source of an object, located at a distance z_o from the the objective lens l_o, can be described as a diverging spherical wave given by:

$$C_1(\overline{r_o})\, Q[z_o^{-1}]\, L[-\overline{r_o}/z_o]. \tag{3.4}$$

Here, $Q[z_o^{-1}] = exp[j\pi z^{-1}\lambda^{-1}(x^2 + y^2)]$ is the quadratic phase function. $L[\overline{r}] = exp[j2\pi(r_x x + r_y y)/\lambda]$ is the linear phase function. λ is the central wavelength of the input light source. $\overline{r_o} = (x_o, y_o)$ is the object point coordinate, and $C_1(\overline{r_o})$ is the complex constant of each object point source. The diverging spherical wave from the object point source experiences the objective lens with the transmission function of $Q[-f_o^{-1}]$, where f_o is the focal length of the lens [2]. Hence, the complex amplitude of the field after passing through the objective lens becomes:

$$C_1(\overline{r_o})\, Q[z_o^{-1}]\, L[-\overline{r_o}/z_o] \;\times\; Q[-f_o^{-1}] \tag{3.5}$$

The field propagates further to the GP lens placed at a distance z_{obj-gp} from the objective lens. As the field passes through the GP lens, the transmission function is expressed as:

$$\big(Q\big[-f_{gp}^{-1}e^{j\delta/2}\big] + Q\big[f_{gp}^{-1}e^{-j\delta/2}\big]\big)/2 \tag{3.6}$$

The GP lens transmission function has has two terms, one for the lens with the focal length f_{gp} and the positive phase shift of $\delta/2$. Conversely, another term is described with the focal length of $-f_{gp}$ and the phase shift of $-\delta/2$. Here, δ is the total phase-shifting value. After the GP lens, a relay lens is placed which enhances the fringe pattern visibility by flattening the wavefronts, since the resultant wavefront curvatures for both waves after passing through the GP lens is large and hence the interference pattern is hard to observe. The field then propagates to the image sensor where the two-wave interference is recorded, each of which has a different wavefront curvature. As a single object point source generates the Fresnel hologram, the entire hologram can be generated from the group of object points in 3D space. A four-step phase-shifting technique is utilized to properly extract the complex hologram, U_H after eliminating bias and twin-image noise.

3.3.2 Jones Matrix for calculating Phase-shift

The geometric phase gain according to the relative rotation angle Ω between the linear polarizer and the micro-polarizer array on the polarized camera is analyzed using the Jones matrix calculation [1]. To simplify the model, we consider the linearly polarized wave after the first polarizer. Then the polarization states after the GP lens are the RHCP and LHCP states with equal amplitude, each of which is $exp(i\Phi)[1, i]^T$ and $exp(-i\Phi)[1, -i]^T$, respectively. Here, Φ is the phase modulation results due to the GP lens, which is the quadratic phase profile of positive and negative lens, and T is the transpose of the matrix. These beams propagate to the linear polarizer with arbitrary angle omega, which is represented as $[\cos^2\Omega,\ \cos\Omega\sin\Omega;\ \cos\Omega\sin\Omega,\ \sin^2\Omega]$ by Jones matrix representation. Then, the horizontal and vertical components of the field are represented as:

$$\begin{bmatrix} E_x \\ E_y \end{bmatrix} \propto \begin{bmatrix} \cos^2\Omega & \cos\Omega\sin\Omega \\ \cos\Omega\sin\Omega & \sin^2\Omega \end{bmatrix} \left(\begin{bmatrix} 1 \\ i \end{bmatrix} exp(i\Phi) + \begin{bmatrix} 1 \\ -i \end{bmatrix} exp(-i\phi) \right)$$

$$\begin{bmatrix} E_x \\ E_y \end{bmatrix} = cos(\Omega + \Phi) \begin{bmatrix} cos\,\Omega \\ sin\,\Omega \end{bmatrix} \tag{3.7}$$

The final intensity of the image is calculated as:

$$I = |E_x|^2 + |E_y|^2 \propto 1 + cos\,(2\Omega + 2\Phi) \tag{3.8}$$

3.3.3 Selection of Phase-Measurement Technique

There are various types of phase measurement algorithms. A common algorithm for phase calculation is the four-step, or four-bucket method given by Wyant in 1982 [32]. In this case, the four recorded set of intensities have a phase separated by 0, $\frac{\pi}{2}$, π, $\frac{3\pi}{2}$ respectively. The phase at each point can be given as:

$$\Phi(x,y) = \tan^{-1}\left(\frac{I_4(x,y) - I_2(x,y)}{I_1(x,y) - I_3(x,y)}\right) \tag{3.9}$$

In four-step phase shifting method, the parameter Ω is set to 0°, 45°, 90°, and 135°, which corresponds to phase shifting of intensity images in 90° step given by the Pancharatnam-phase effect. The final hologram U_H without bias and twin image noise is obtained in Eq. (3.10), where I_k is the consecutive intensity images for each relative rotation between the polarizer and the polarized image sensor in $\Omega = 45°$.

$$U_H = (I_3 - I_1) - i(I_2 - I_0) \tag{3.10}$$

The relative phase difference is of $\pi/2$. By changing the relative angle between the two polarizers, the amount of geometric phase gain is controlled. This can also be described by the Jones Matrix method as discussed in Section 3.3.2. However, even with this phase-shifting method, the real time acquisition of a clear hologram is hard to achieve. If the object moves faster than the time period of the entire phase-shifting process, then the acquired and reconstructed hologram image would

be blurred or nothing will be observed. A simple solution to this problem is to replace the second polarizer and the general image sensor by a single polarized image sensor, such that the micro-polarizer is attached on every sensor pixel. By doing so, the motionless single-shot phase-shifting digital holography can be achieved. This spatial division phase-shifting method is referred as a parallel phase-shifting [31], and widely used in various digital holography systems.

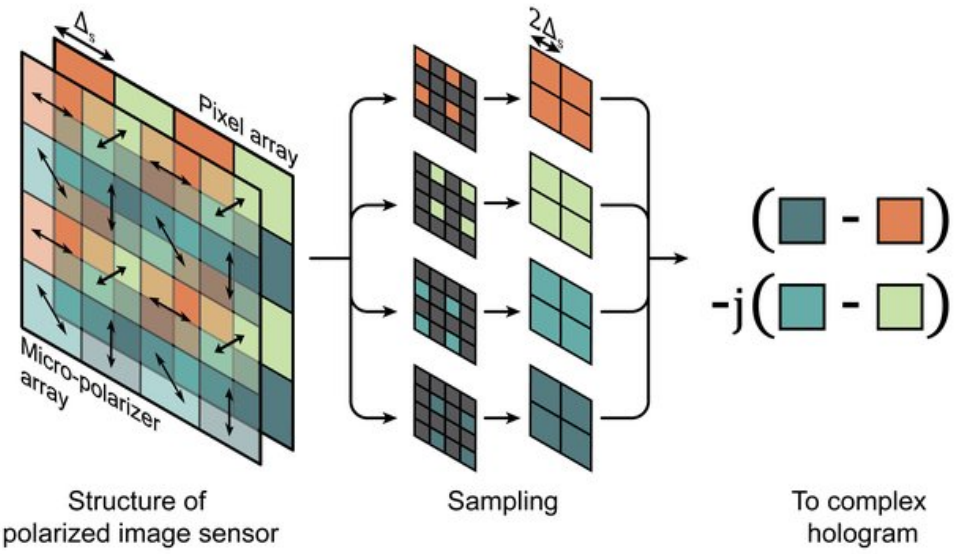

Figure 3.6: Illustration of parallel phase-shiting method. The structure of polarized image sensor shows that 4 pixels combine to make one complex hologram pixel [2].

The structure of a polarized image sensor is shown in Fig. 3.6 [2]. The micro-polarizer array attached to the pixel array can be arranged to be rotated by an interval of 45°with the adjacent micro-polarizer. Therefore, the intensity values of the polarization component of 0°, 45°, 90°, and 135° of light incident on the 2×2 array of pixel group are simultaneously recorded. Once the raw image file is obtained from the polarized image sensor, the four phase-shifted images are extracted with a proper sampling method. The sampled period of the phase-shifted images is considered as twice of the original pixel size as shown in Fig. 3.6. The four phase-shifted images, each of which has the defined hologram intensity are recombined into the Complex-

valued Hologram (CH) as [10],

$$CH[p,q] = \big(H_3[p,q] - H_1[p,q]\big) - j\big(H_4[p,q] - H_2[p,q]\big) \tag{3.11}$$

Here, $H_{1,2,3,4}$ correspond to the phase shifted images with $\delta = 0°$, $90°$, $180°$, and $270°$, where the relative rotation angles between the first polarizer are $0°$, $45°$, $90°$, and $135°$, respectively. p and q are the pixel indices of the two-dimesional array data. Then, the object field can be retrieved by using the conventional Fresnel back propagation method, that is to correlate $CH[p,q]$ with the quadratic phase function which is given by:

$$Q[-z_{rec}^{-1}; p, q] = exp\bigg[- \frac{j\pi}{\lambda_{rec}}\big(p^2\Delta_x^2 + q^2\Delta_y^2\big)\bigg] \tag{3.12}$$

Here, z_{rec} is the reconstruction distance which is the topic of the next section 3.4 and is discussed in detail below. λ is the central wavelength of light, $\Delta_{x,y}$ is the width and height of the sampling grid, respectively.

3.4 Methodology for Reconstructing Images

The reconstructed wave field U_R on (x, y) domain is retrieved by Fresnel transformation under the wavelength λ, by convolving the complex hologram CH, given by Eq. (3.10), on (ξ, η) domain with the quadratic phase parameterized by the reconstruction distance $z_{rec}(\lambda)$ given by the following equation:

$$U_R(x, y, z_{rec}; \lambda) = CH(\xi, \eta; \lambda) \ \otimes \ exp\bigg[i\frac{2\pi}{\lambda}\bigg(\frac{\xi^2 + \eta^2}{2\, z_{rec}(\lambda)}\bigg)\bigg] \tag{3.13}$$

As mentioned earlier, the four phase-shifted images, each of which has the defined hologram intensity are recombined into a single complex-valued hologram (CH). Using the RSD integral or the Angular Spectrum (AS) method [33] which are both exact solutions for the nonparaxial regime, wave field propagation of light waves can

be achieved which is discussed below in sub-section 3.4.1. Later, the formula for reconstruction distance is calculated in sub-section 3.4.2.

3.4.1 Angular Spectrum Method

The AS method is an efficient way for propagating wave fields. This method treats light as a superposition of plane waves of different wave vectors and uses a Fourier transform to compute the light fields in the spatial-frequency domain. A Fast Fourier Transform (FFT) based AS method can have a high calculation speed and can be used for both parallel and arbitrarily oriented planes [34]. The fast Fourier transform is a mathematical method for transforming a function of time into a function of frequency by computing the discrete Fourier transform of a sequence or its inverse. AS method handles the initial light field and its propagation in the spatial-frequency domain.

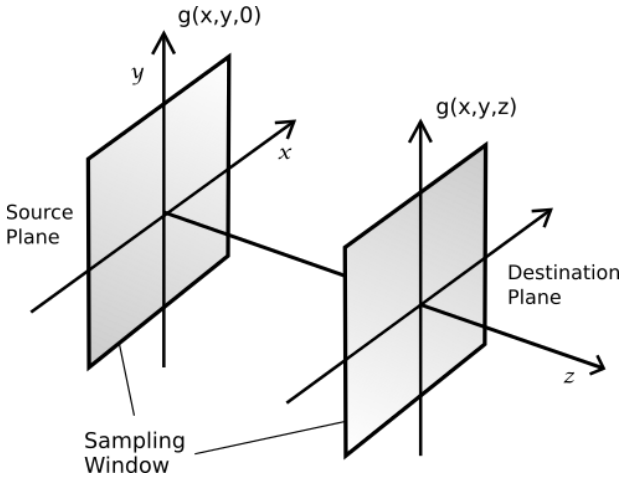

Figure 3.7: Propagation of a wave field from the source plane: g(x,y,0) to destination plane: g(x,y,z) while sampling.

Figure 3.7 shows a graphical description of wave field propagation. The propagation of light from $U(x_1, y_1, z_1)$ to $U(x_1, y_1, z_2)$ can be given as:

$$A(\alpha, \beta, z) = A(\alpha, \beta, 0)\, G(\alpha, \beta, z) \tag{3.14}$$

where $A(\alpha, \beta, z)$ is the Fourier transformation of the light field at distance z. $G(\alpha, \beta, z)$

is the Fourier transform of the Huygens wave.

$$A(\alpha, \beta, z) = F\{U(X, Y, Z)\} \tag{3.15}$$

$$U(X, Y, Z) = F^{-1}\{A(\alpha, \beta, z)\} \tag{3.16}$$

$$G(\alpha, \beta, z) = exp\big(i\sqrt{k^2 - \alpha^2 - \beta^2}\, z\big) \tag{3.17}$$

Traditionally, the properties of the AS method have been investigated extensively for the case of non-paraxial on-axis wave propagation. [35]. However, it was reported that AS is not suitable for longer propagation distances due to the numerical errors. Reference [36] shows that the numerical error depends on the computational window size, while providing guidelines for accurate computation. Zero padding of the input field in the spatial domain is a suitable choice to reduce the numerical errors. This also solves wave-propagation between tilted planes [34]. However, the zero-padding procedures for all classes of AS methods results in higher memory requirements as well as higher computational effort. The limitations of the computing capacity leads to limiting the maximum window size and, therefore, the available amount of zero padding to be used. Hence, measures to reduce the computational efforts and its memory are highly desirable [33].

In a work by *Tomasz et al.* [33], a modified AS algorithm is proposed that evaluates only the non-zero components of the field. This enables an accurate and efficient field computation for cases where the conventional AS method cannot be implemented. For propagating wave fields to any distance along the *z-axis*, a Wigner Distribution (WD) of the AS propagation method is presented. The zero padding procedure increases the number of frequency samples in the signal spectrum and can be understood as a Fourier interpolation. An advantage of this method is that for the calculation of wave field $u[z_0]$, it is not necessary to compute all spectral components because the field is broken down into individual blocks of size $(M) \times (N)$. This requires less

computational memory and enables calculation of large scale field on systems with an ordinary amount of computational memory, such as personal computers [37] making it more feasible to use this technique for reconstruction of images from the complex hologram, CH at any given propagation distance, z_{rec} which is calculated below.

3.4.2 Formula for Reconstruction Distance

A numerical reconstruction distance is derived from the focal length of the GP lens, f_{gp}. The focal lengths of the GP lens is wavelength dependent. Therefore, a fluorescence bandpass filter with a center wavelength of 520 nm is used such that, the wave field before passing through the GP lens has a higher monochromaticity contributing to a single focal length. By using Eq. 2.4, the focal length of the GP lens used here, f_{gp} is calculated to be 100.5 mm at 520nm. Mathematically, the focal length of the GP Lens can be calculated as follows:

$$f_{gp}(\lambda) = f_{ref}\left(\frac{\lambda_{ref}}{\lambda}\right) \tag{3.18}$$

where λ_{ref} is the wavelength that was used for the fabrication of the GP lens, and f_{ref} is the corresponding focal length.

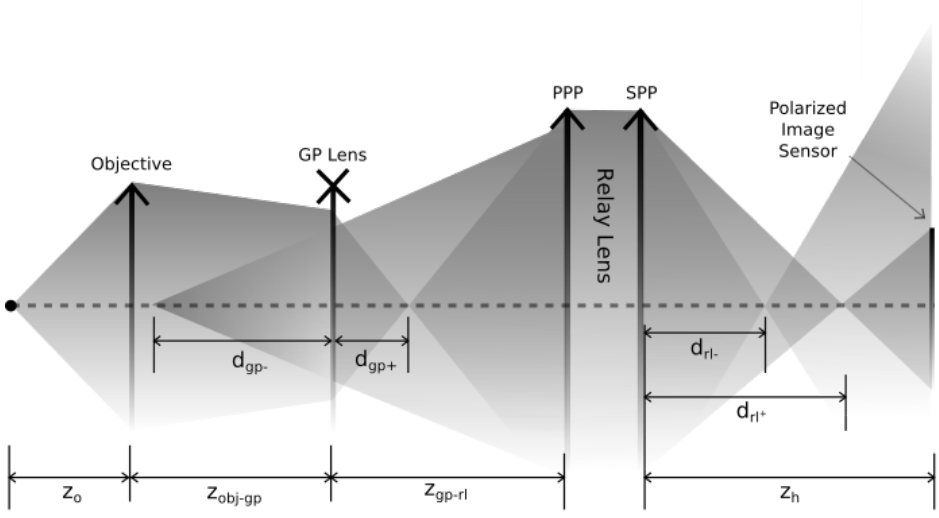

Figure 3.8: System parameters schematic for finding the reconstruction distance, z_{rec}.

A schematic of the system illustrating the various parameters is shown in Fig. 3.8. Once f_{gp} is determined, the imaging distance after the objective lens and the GP lens is calculated. The system parameters include z_o as the object distance, z_{obj-gp} as the distance between the objective and the GP Lens. z_{gp-rl} is the distance between the GP Lens and the relay lens (primary principal plane, PPP) and z_h is the distance between the relay lens (secondary principal plane, SPP) and the image sensor. $d_{gp}^{\pm}$ is the GP imaging distance due to positive and negative focal lengths respectively. $d_{rl}^{\pm}$ is the relay lens imaging distance from the SPP. After calculating $d_{gp}^{\pm}(\lambda)$ and $d_{rl}^{\pm}(\lambda)$ using the equations given below, we can finally calculate the numerical reconstruction distance as Eq. 3.21.

$$d_{gp}^{\pm}(\lambda) = \left(\frac{\pm z_{obj-gp} f_{gp}(\lambda)(z_o - f_o) \mp f_o f_{gp}(\lambda) z_o}{(z_{obj-gp} \mp f_{gp}(\lambda))(z_o - f_o) - f_o z_o} \right) \tag{3.19}$$

$$d_{rl}^{\pm}(\lambda) = \left(\frac{f_{rl}(z_{gp-rl} - d_{gp}^{\mp}(\lambda))}{z_{gp-rl} - d_{gp}^{\pm}(\lambda) - f_{rl}} \right) \tag{3.20}$$

$$z_{rec}^{\pm}(\lambda) = \frac{(z_h - d_{rl}^{\mp}(\lambda))(d_{rl}^{\pm}(\lambda) - z_h)}{\pm \Delta d_{rl}} \tag{3.21}$$

Using these formulas, all the variables can be modulated to calculate the reconstruction distance for any object distance. This enables to input the z_{rec} value for the modified AS algorithm discussed in sub-section 3.4.1, and consequently the reconstruction at a particular image plane can be achieved. Chapter 4 discusses the system characterization for the modified GP-SIDH system.

CHAPTER 4: SYSTEM CHARACTERIZATION

In this chapter, the optical components of the modified GP-SIDH system is characterized. The experiments conducted for this purpose are detailed here followed by their corresponding results which are then interpreted as observations.

4.1 Experimental Setup

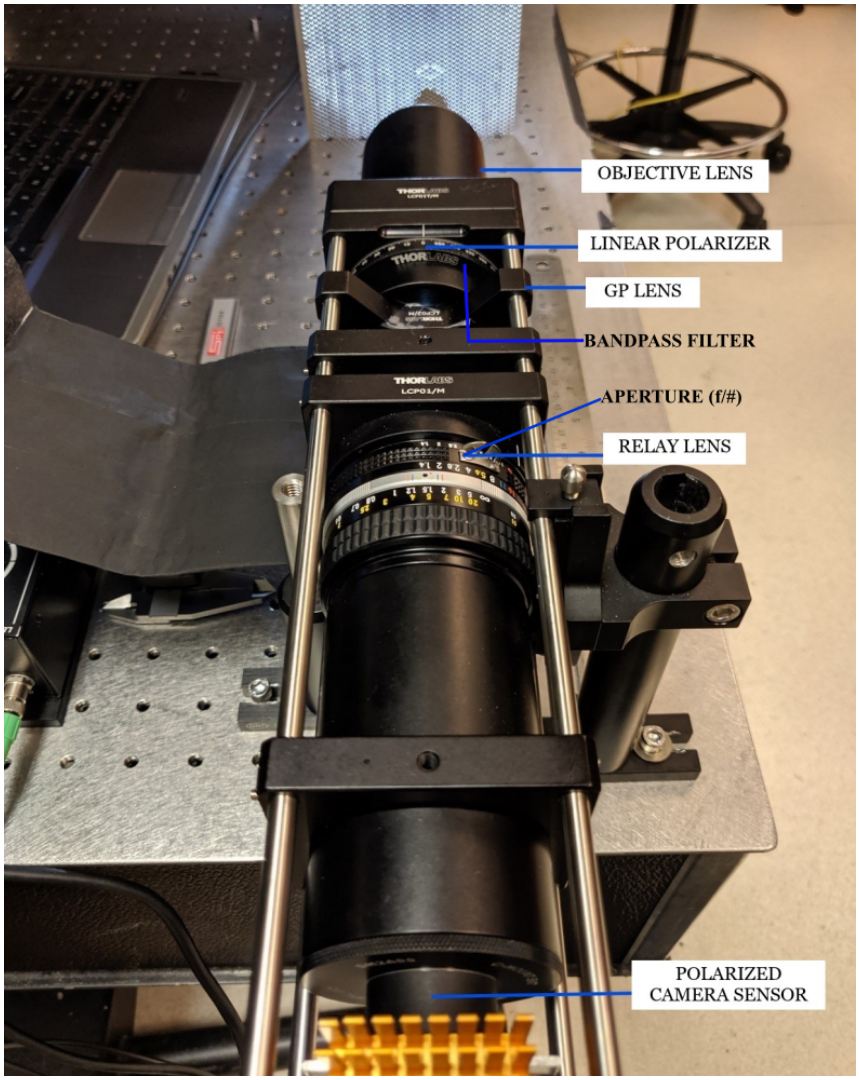

Figure 4.1: An image of the modified GP-SIDH system apparatus.

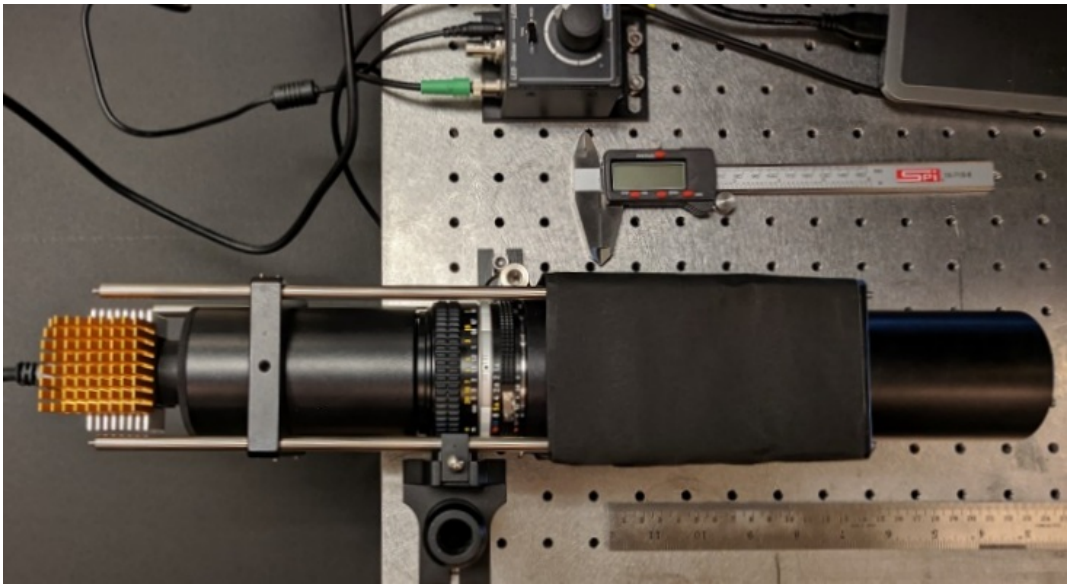

Figure 4.2: Top-view image of the modified GP-SIDH system apparatus.

Figure 4.1 and 4.2 shows the image of the system architecture for the modified GP-SIDH system. The basic idea about experimental setup is similar to system proposed by *Ki-Hong Choi et al.* [1] as mentioned in section 3.2. The values of some parameters stay unchanged for any experiment unless otherwise stated. These distances are selected carefully after carrying out experiments designed to evaluate these parameters based on the quality of the interference pattern on the image sensor. These are as follows:

1. Focal length of the convex objective lens, $f_o = 100$ mm.
2. Focal length of the GP lens, $f_o = 100.5$ mm.
3. Focal length of the Relay lens, $f_{rl} = 50$ mm.
4. Thickness of the Relay lens, $t_{rl} = 41$ mm.
5. Distance between the objective lens and the GP lens, $z_{obj-gp} = 75.04$ mm.

Some other parameters as mentioned below, are variable depending on the type of experiment being carried out.

1. Distance between an object plane and the objective lens, z_o ranges from 100 mm to 350 mm.

2. Distance of GP lens from PPP of the Relay lens, z_{gp-rl} varies between 55 mm and 63 mm.

3. Distance of image sensor from the SPP of the Relay lens, z_h varies between 110 mm and 119 mm.

4. Aperture size of the Relay lens, given by the f-number which is f_{rl}/D_{EP}, varies from f/1.4 to f/16. Here, D_{EP} is the effective diameter of the entrance pupil.

Based on all the parameters discussed above, experiments were designed to analyze the function of each component and establish a relationship between various quantities. The total optical path length (OPL) of the system is under 300 mm. First, the GP-SIDH apparatus was set up such that a digital complex hologram can be recorded in a computer and the image of the given object can be reconstructed in real-time using the modified AS propagation method, provided the reconstruction distance, z_{rec} is known beforehand using Eq. (3.21). The experiments that were conducted are stated below:

1. Quantifying the parameter *Defocus* and evaluating its effects on the quality of the reconstructed image.

2. Quantifying the effects of varying object distance, z_o, for a given f-number on image reconstruction quality.

3. Comparing the effects of various window functions on removing the parasitic signals from a reconstructed image and selecting the best window function.

4. Evaluating the variation of pixel area over which the reconstructed image is visible for a range of f-numbers.

5. Measuring a 3D object such as a figurine, to evaluate overall system performance for recording and reconstruction.

4.2 Results and Observations

In this section, the three-dimensional recording and simultaneous reconstruction capability of the modified GP-SIDH system is demonstrated. Recording and reconstruction results are presented consecutively. An object is illuminated with incoherent light which after passing through the system forms a complex hologram on the monochromatic polarized image sensor (BFS-U3-51S5P-C Blackfly® S GigE, FLIR). To overcome the problems of overexposure or underexposure, an algorithm is used to generate a digital HDR hologram.

Initial exposure time for capturing an image, growth factor and the number of images are the three parameters required to generate a 8-bit *.bmp* format HDR holographic image. This is carried out after capturing a chosen number of images of the scene each with varying exposures according to the initial exposure time and the growth factor. The pixel resolution of the polarized camera is 2448 $\times$ 2048. However, only the central 2048 $\times$ 2048 pixels are utilized for the simplicity. Both horizontal and vertical pixel size of the image sensor is 3.45 μm. But to sample the complex hologram data, the sampling period has been regarded as twice of the original pixel size, which is 6.9 μm, and the sampling number is 1024 $\times$ 1024 pixels. The bit-per-pixel or the bit-depth of the sensor is set to 8-bit, which implies that the obtained signal is sampled and stored with 256 levels after correcting for the dynamic range. The polarized sensor is connected to the computer with a GigE Vision to USB 3.1 interface. The maximum frame rate of the sensor is 75 frames per second, when the pixel resolution is set as 2048 $\times$ 2048. The noise from all the random light sources entering the system from the lateral direction needs to be minimized for the system to perform optimally. The modified GP-SIDH system is configured using lens tubes of required length to control the light entering the system and most importantly, the

GP lens has been covered from all the lateral sides as it is the most sensitive part of the system. Various experiments are carried out as per the described procedure and their results are discussed in the subsection below.

4.2.1 Experimental Evaluation

EXPERIMENT 1: Quantifying the parameter *Defocus* and evaluating its effects on the quality of the reconstructed image. The position of the Secondary Principle Plane (SPP) of the relay lens with respect to the image sensor, z_h along with the distance of the Primary Principle Plane (PPP) from the GP lens determines if the interference fringes are perfectly in focus on the image sensor or not. Choosing the optical distances such that the perfectly-focused Fresnel rings are observed on the computer screen, produces a degraded reconstruction result which is validated below. The experiment was conducted after placing optical components of the system as shown in Fig.4.3.

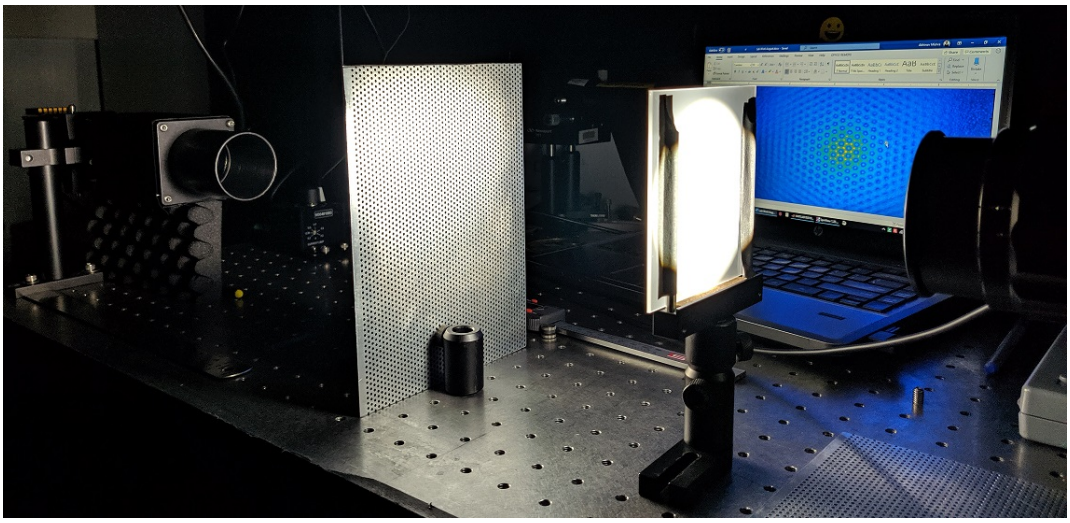

Figure 4.3: Experimental Setup for the defocus test runs with the modified GP-SIDH system apparatus.

An object is placed at a fixed distance such that the parameter, $z_o = 276.53\,mm$. The distance between the objective lens and the GP lens, z_{obj-gp} is fixed at 75.04 mm. The aperture size for all the test runs is fixed at f/1.4. The parameter z_{gp-rl} is

varied between 55 mm and 63 mm based on the test run. Consequently, z_h also varies between 110 mm and 119 mm. There are two ways to defocus from the perfect rings position. Either by moving the relay lens towards the polarized image sensor or by moving the image sensor towards the relay lens. Both of these methods were evaluated and conclusively, the former option was selected as the basis for this experiment. Table 4.1 below captures the values of important parameters for a number of test runs.

Table 4.1: Distances used to quantify the parameter "Defocus" for every test run (All distances in mm).

Test Run	z_{gp-rl}	z_h	z_{rec}	% Defocus
1	62.33	110.83	90.542	0
2	61.77	111.39	90.485	7.65
3	60.99	112.17	90.396	18.31
4	60.55	112.61	90.341	24.32
5	60.02	113.14	90.270	31.56
6	59.42	113.74	90.182	39.75
7	58.93	114.23	90.106	46.44
8	58.22	114.94	89.987	56.14
9	57.78	115.38	89.908	62.16
10	57.25	115.91	89.808	69.40
11	56.29	116.87	89.614	82.51
12	55.51	117.65	89.442	93.16
13	55.01	118.15	89.325	100

To quantify the measure of defocus with varying test runs, all the other parameters were kept at a constant value and only the position of the two principle planes of the relay lens with respect to the image sensor and simultaneously the GP lens was

changed. Firstly, the distances were adjusted such that perfectly focus of the interference rings patterns was observed. This was marked as 0% *Defocus*. A perforated aluminum sheet was illuminated with transmissive diffused light was used as an object. Defocus is introduced in the system by moving the principle planes of the relay lens. Starting at 0% *Defocus*, the distances are changed slightly and the digital hologram is recorded and reconstructed for each test run until 100% *Defocus* is achieved when the position of the relay lens cannot be moved any further as per the system design. At 0% Defocus, placing the object at 276.53 mm from the objective lens, predicted the reconstruction distance given by Eq. (3.21) as $z_{rec} = \pm\, 90.542\, mm$. It was observed that the reconstruction for this test resulted in a degraded image with negligible information about the object as shown in Figure 4.3.

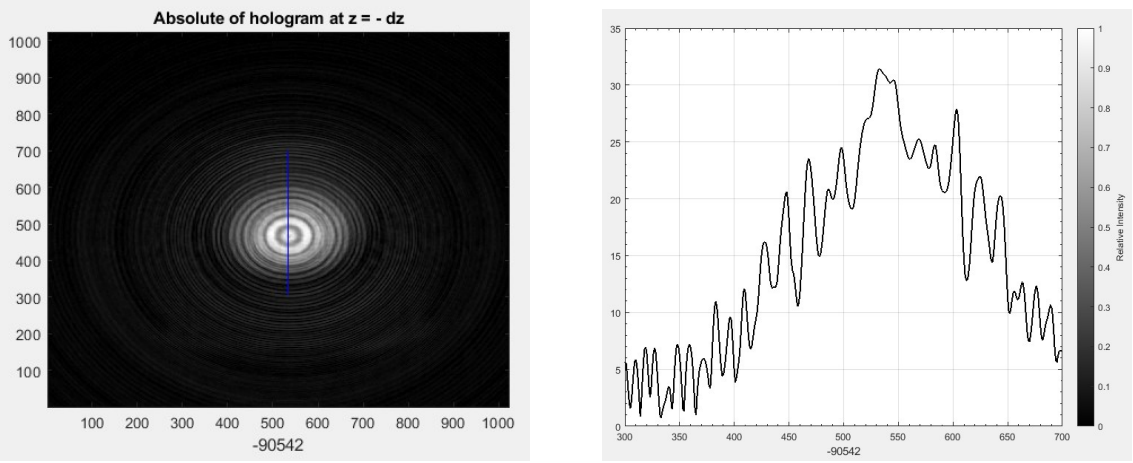

(a) Reconstructed Image

(b) Intensity Profile for the vertical line in (a)

Figure 4.4: Test Run 1 reconstruction results for a perfectly focused interference rings pattern hologram. Image (a) depicts the absolute image of the hologram at $-\, z_{rec}$ and Image(b) shows the relative intensity profile for the marked section.

The digital holograms were recorded and reconstructed simultaneously for every test run with varying percentage of defocus. For identifying the optimum defocus condition, the reconstructed images were analysed and compared based on the following criterion:

1. The maximum area of image where the reconstructed object is visible.

2. The relative intensity curves having a maximum contrast such that the maximum and minimum intensity ratio for each peak is higher.

3. The Full Width at Half Maximum (FWHM) value should be higher for each of the peaks corresponding to the relative intensity profiles.

The reconstruction quality of the image from test run 2 until test run 8 was analyzed. These images lacked at least two out of three criterion mentioned above to qualify as a good reconstruction. Furthermore, test run 12 and test run 13 satisfied the first criterion, but the contrast and FWHM values clearly indicated that these were not the best possible case. Eliminating these, we are now left with test run 9, 10 and 11. These runs satisfied all three criterion to some extent to be considered as good reconstruction. Although, to find the best ones among these, further scrutiny was required. The reconstruction result for test run 10 has comparatively the lowest contrast among these three and hence was eliminated. This leaves us with test run 9 and 11, both of which are analyzed below:

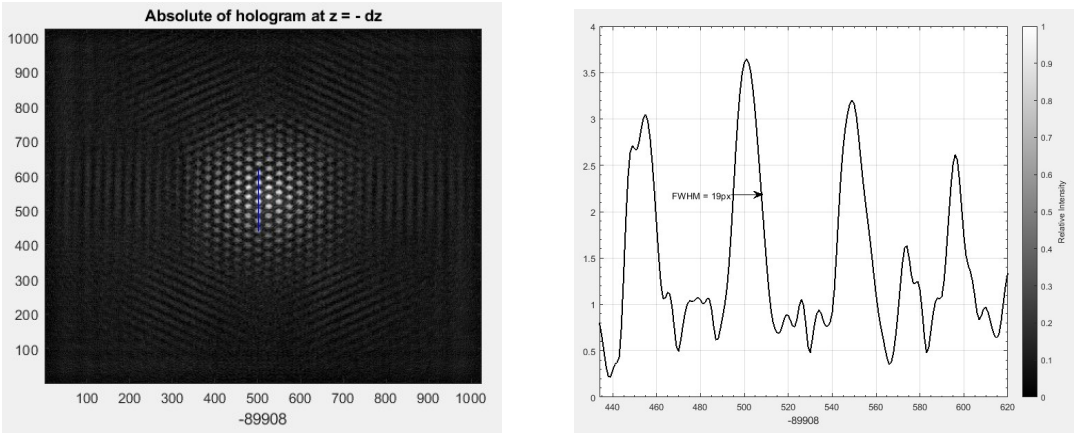

(a) Reconstructed Image

(b) Intensity Profile for the blue vertical line marked in (a).

Figure 4.5: Reconstruction results for test run 9. Image (a) depicts the absolute image of the hologram at $-z_{rec}$ and Image(b) shows the shows the relative intensity profile for the marked section.

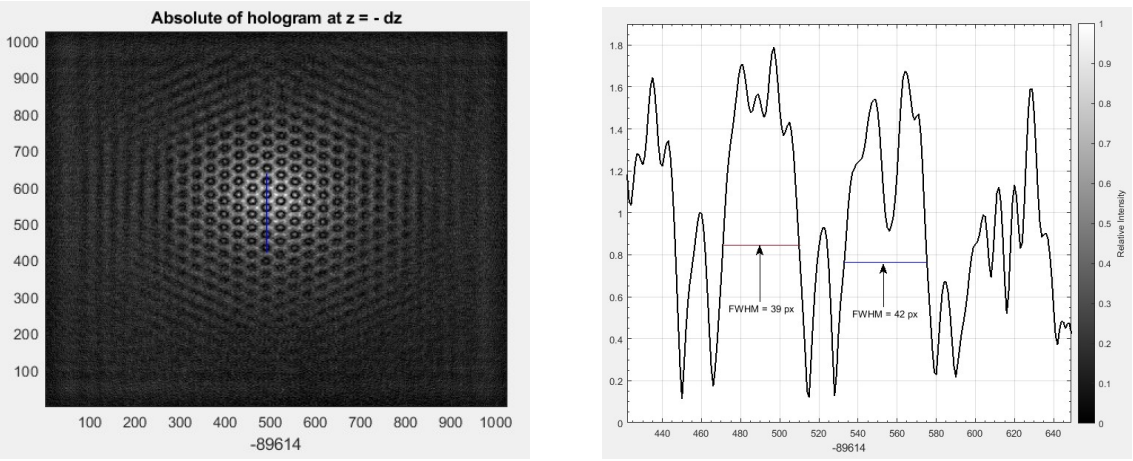

(a) Reconstructed Image

(b) Intensity Profile for the blue vertical line marked in (a).

Figure 4.6: Reconstruction results for test run 11. Image (a) depicts the absolute image of the hologram at $-z_{rec}$ and Image(b) shows the shows the relative intensity profile for the marked section and the FWHM value of two of its peaks resembling the two points at that location.

Based on the results shown in Figure 4.4 and Figure 4.5, although the peak intensity value is greater for test run 9, the level of contrast and the FWHM value is lower than that of test run 11. Also, the reconstructed image for test run 11 clearly shows the perforated holes for the meshed aluminum sheet, whereas test 9 shows us the reconstructed image of the light source behind the object. Both of these test runs can generate good reconstructed images from the complex holograms. However, based on this experiment, the parameters used for test run 11 which is at 82.51% defocus distance from the perfectly focused interference rings is selected as the optimum defocus distance for the best reconstruction of a given object.

EXPERIMENT 2: Quantifying the effects of varying object distance, z_o, for a given f-number on image reconstruction quality. The same criterion as above is used to identify the bounds along the z-axis where the reconstruction is optimal. For this experiment, all the system parameters were kept at a constant value except for the object distance for every test run, unless otherwise stated. The experimental setup

is shown in Fig. 4.7 & 4.8.

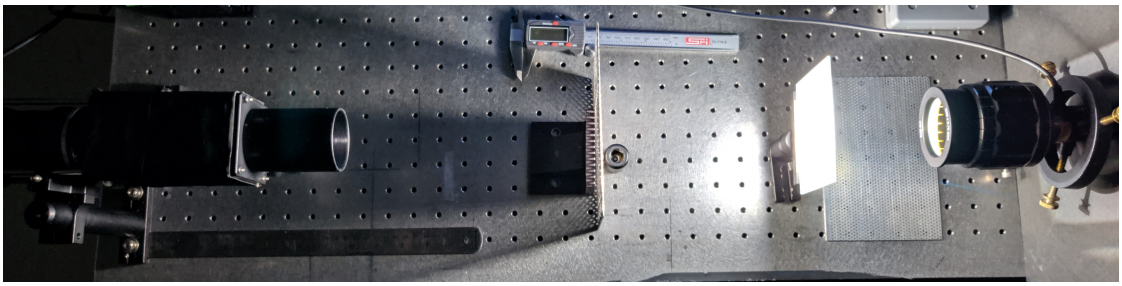

Figure 4.7: Top View of the setup for experiment 2 with the modified GP-SIDH system apparatus.

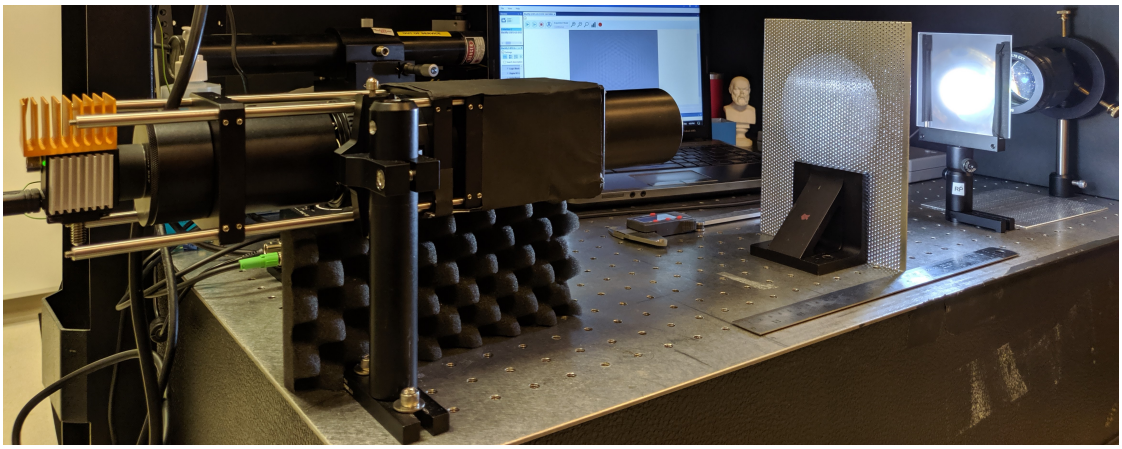

Figure 4.8: Side View of the setup for experiment 2 with the modified GP-SIDH system apparatus.

For the object, we have the same perforated aluminum sheet which is illuminated using a set of diffused LED lights such that it is transmissive to the system. The distance between the object plane and the first converging lens, z_o, varies between 89.53 mm and 391.53 mm. The parameter z_{obj-gp} is set as 75.04 mm. z_{gp-rl} varies from 60.47 mm to 62.33 mm depending on the *defocus* percent value lying between 67% and 90% with respect to each object distance. This was done to ensure that we have optimum defocus for every object distance. The intensity profiles for the every reconstructed image from the corresponding digital hologram is compared relatively to find the bounds for optimum object distance, z_o.

Table 4.2: System Parameters for Experiment 2 (All distances in mm).

Test Run	z_o	z_{gp-rl}	% Defocus
1	89.53	55.88	89.28
2	166.53	57.67	67.24
3	190.53	57.38	70.81
4	216.53	56.43	82.51
5	266.53	56.23	84.97
6	391.53	55.81	90.14

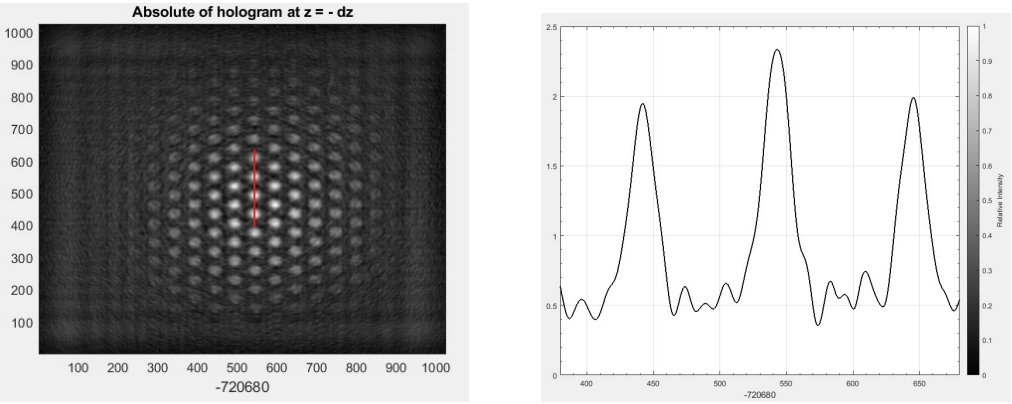

Figure 4.9: Reconstruction results for test run 1 and the relative intensity profile for the marked section.

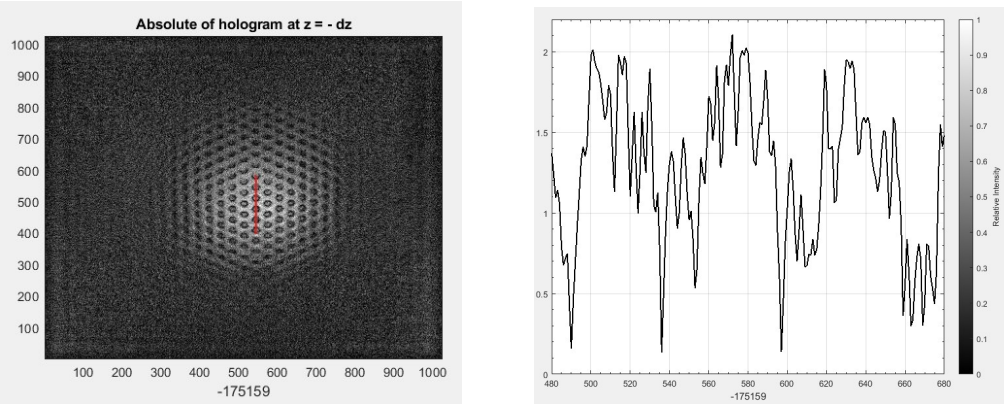

Figure 4.10: Reconstruction results for test run 2 and the relative intensity profile for the marked section.

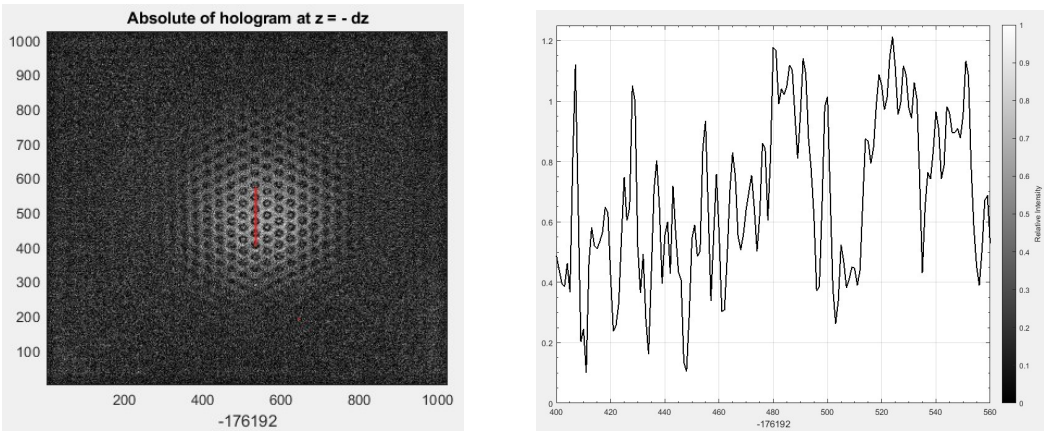

Figure 4.11: Reconstruction results for test run 3 and the relative intensity profile for the marked section.

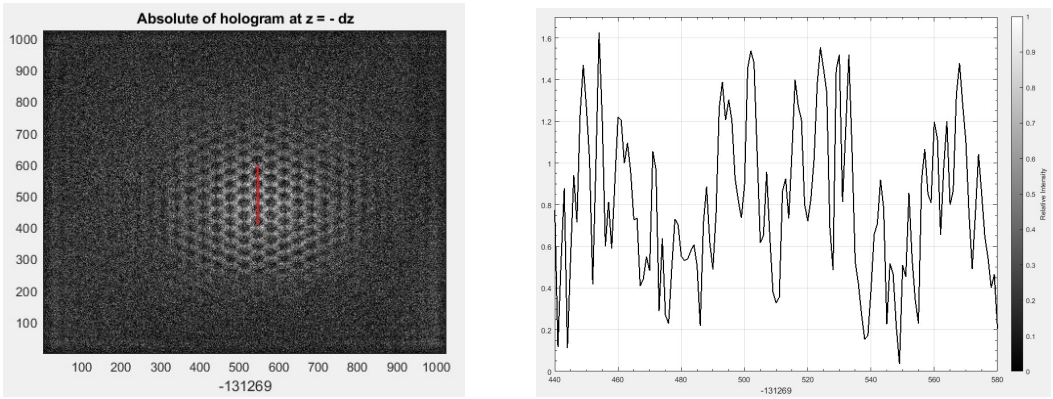

Figure 4.12: Reconstruction results for test run 4 and the relative intensity profile for the marked section.

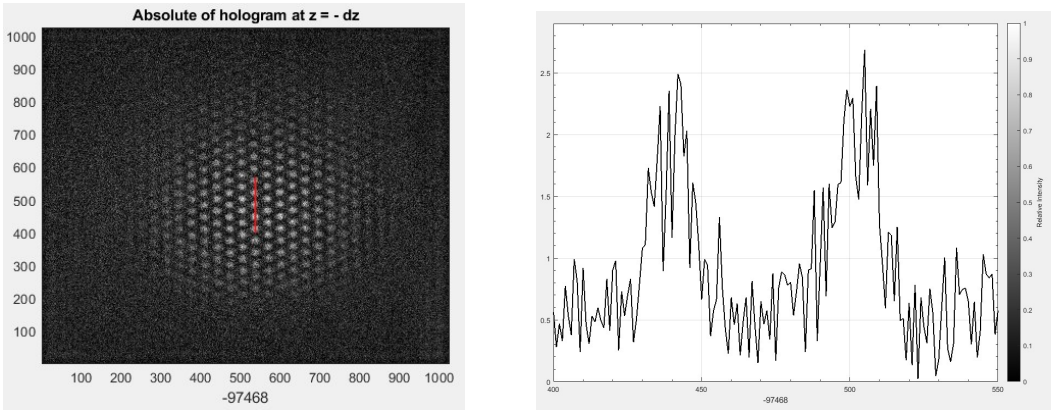

Figure 4.13: Reconstruction results for test run 5 and the relative intensity profile for the marked section.

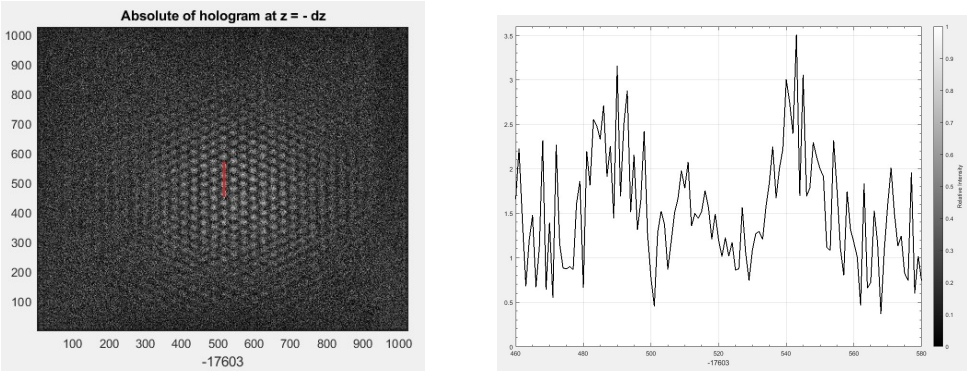

Figure 4.14: Reconstruction results for test run 6 and the relative intensity profile for the marked section.

The results for all the test runs are shown in Fig. (4.9 - 4.14). The reconstructed hologram is shown above along with its corresponding intensity profile across the red line marked on the hologram. The same set of points are evaluated in each test run and compared amongst each other based on the set of criterion mentioned in experiment 1. We can observe that after increasing the object distance the hologram tends to be more noisy. Note that there is no window function applied for the above reconstructed holograms. Also the source of light is kept at a constant distance from the apparatus. From the intensity profiles, we can note that with increasing object distance, the maximum relative intensity starts decreasing until test run 3 and then it increases as the object is moved away from the apparatus and closer to the light source. The area of the reconstructed image for all the test runs stays nearly the same because the f-number is kept at a constant value. Test runs 1, 2 and 3 produce good results meeting all the three criterion. Test run 4 and 5 meet two of the three criterion whereas test run 6 gives a bad result. Hence, objects placed under 200 mm from the objective lens are in the optimal FOV for the system apparatus provided the type of illumination is transmissive.

EXPERIMENT 3: Comparing the effects of various window functions on removing the parasitic signals from a reconstructed image and selecting the best window function. The experiment was conducted after placing the optical components at

distances exactly as that of test run 11 for the *Defocus* experiment given in Table 4.1. The reconstructed image without applying any window function is first shown in Fig. 4.15. The reconstruction results as well as the corresponding intensity profiles for various window functions are shown in Fig. 4.15 - 4.19. These are then compared with each other based on the criteria mentioned in experiment 1.

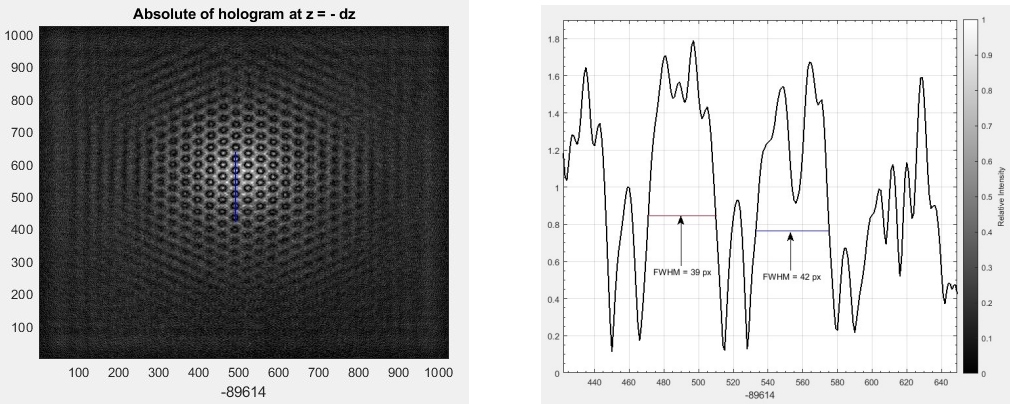

Figure 4.15: Reconstruction results any without window function and the relative intensity profile for the marked section.

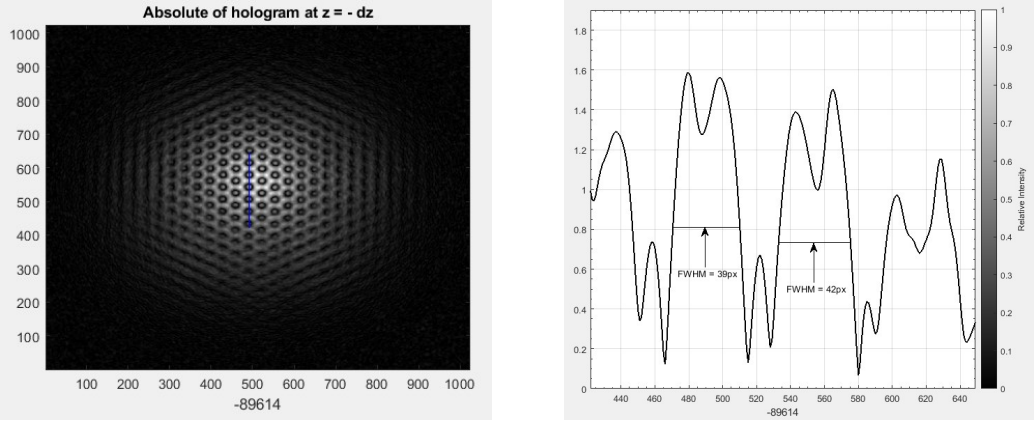

Figure 4.16: Reconstruction results after applying Hamming window function and the relative intensity profile for the marked section.

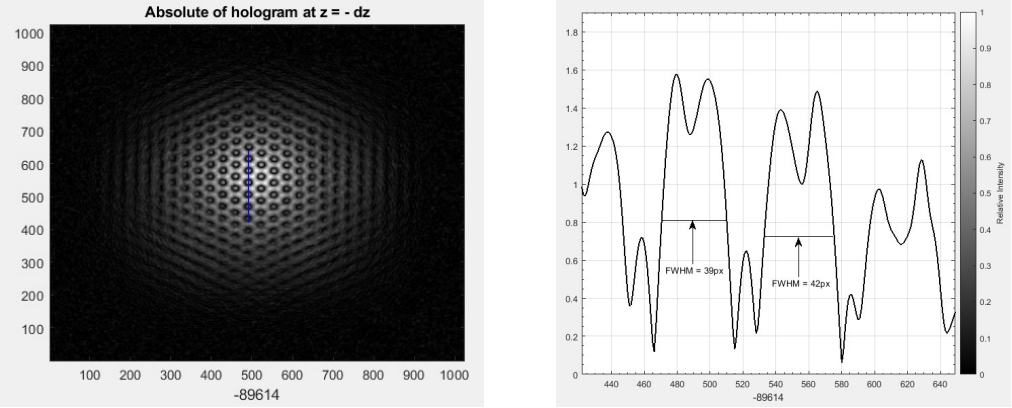

Figure 4.17: Reconstruction results after applying Hann window function and the relative intensity profile for the marked section.

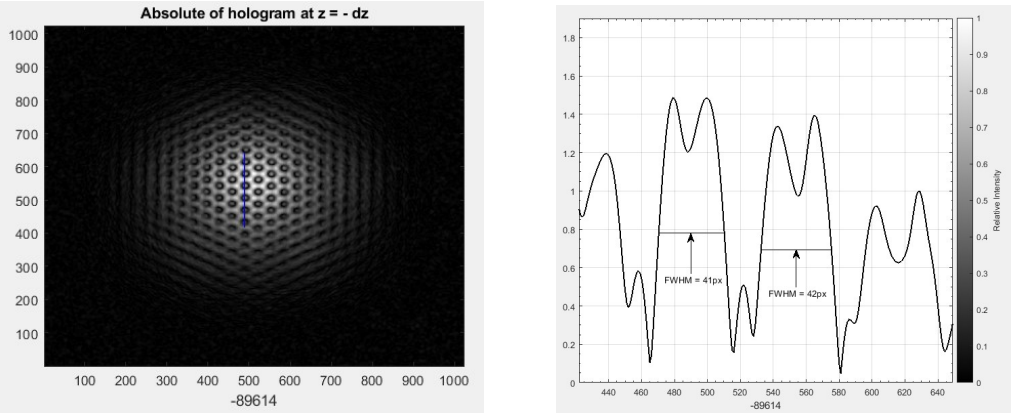

Figure 4.18: Reconstruction results after applying Blackman window function and the relative intensity profile for the marked section.

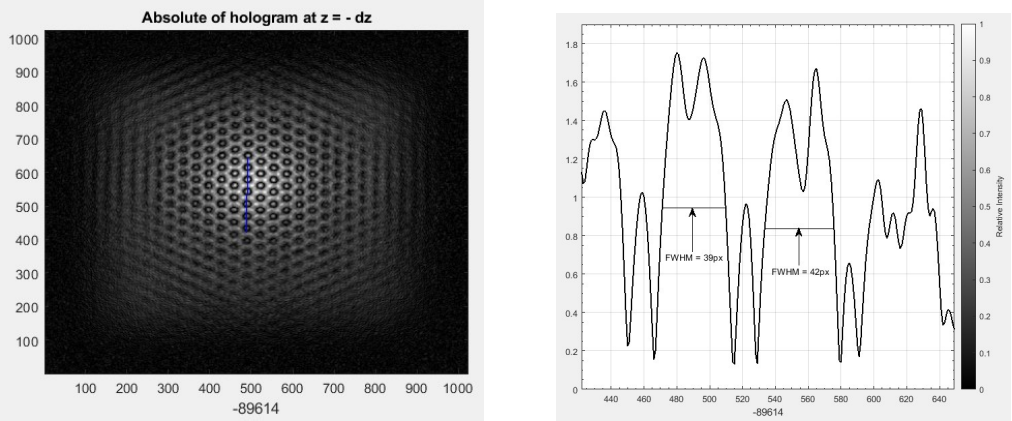

Figure 4.19: Reconstruction results after applying Tukey window function and the relative intensity profile for the marked section.

It can be clearly seen that the Tukey window function which is essentially a tapered cosine function that gives us the best result as it satisfies all the criterion required for a good reconstruction. The maximum area of the reconstructed object is visible with high contrast relative intensity and with no loss in the FWHM values as compared to Figure 4.10 without any window function. Hence, the Tukey window function is used for all reconstruction purposes.

EXPERIMENT 4: Evaluating the variation of pixel area where the reconstructed image is visible over a range of f-numbers (aperture size). The f-number of any optical system is defined as the ratio of the effective focal length of the system to the effective entrance pupil diameter, $f/\# = \frac{EFL}{D_{EP}}$. Variation in the aperture size defines how much of light can be captured by the optical system which subsequently defines the pixel area visible after reconstruction.

Table 4.3: Image reconstruction area for different f-numbers.

$f - number$	Hexagon Side Pixels a	Image Pixel Area $\frac{3\sqrt{3}}{2}a^2$
1.4	268	186604
2	217	122341
2.8	195	98792
4	138	49478
5.6	103	27563
8	82	17469
11	76	15006
16	26	1756

The pixel area for a given image was calculated by individually marking the pixel locations along the x and y axes where the reconstructed image points were visible. For simplicity, the area was approximated as a part of a regular hexagon with given

side length as a and the area as $\frac{3\sqrt{3}}{2}a^2$. The number of pixels along one of the hexagonal sides of the reconstructed image was found which was the used to find the enclosed pixel area. This process was then repeated for several measurements for the same optical parameters over different aperture sizes (f-number). The object distance selected for this experiment, $z_o = 276.53$ mm, $z_{obj-gp} = 75.04$ mm, $z_{gp-rl} = 56.24$ mm and $z_h = 116.9$ mm. The reconstruction distance, z_{rec} for these optical distances is at -89.543 mm. All of the reconstruction is carried out after applying the window function selected in Experiment 3 as Tukey window. Table 4.3 lists the values of pixel area available for reconstruction for different f-numbers.

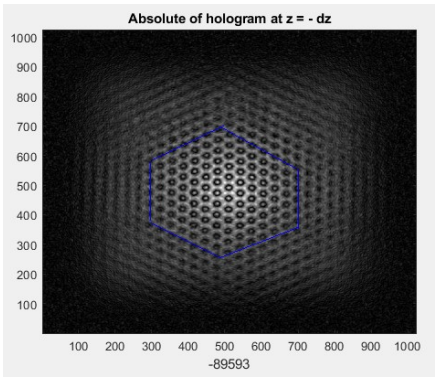

(a) f/1.4

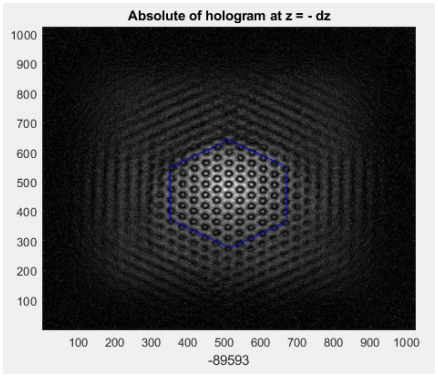

(b) f/2.8

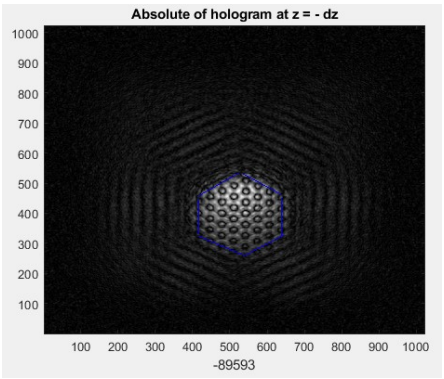

(c) f/5.6

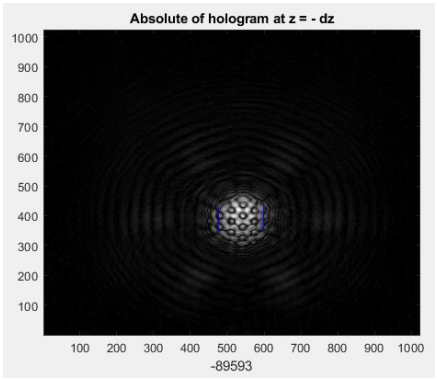

(d) f/11

Figure 4.20: Measuring the reconstructed image pixel area for various aperture sizes.

The reconstruction results are shown in Figure 4.20 above. We can clearly infer based on the above experiment that the reconstructed image area in pixels decreases

with decreasing aperture size (increasing f-number). f/1.4 has the maximum pixel area of 186604 whereas f/16 has the minimum pixel area of 1756.

EXPERIMENT 5: Measuring a 3D object such as a figurine, to evaluate overall system performance for recording and reconstruction. A Socrates figurine is used as an object for this experiment. The object distance, z_o was set as 124.53 m, z_{obj-gp} was constant at 75.04 mm, z_{gp-rl} was set as 55.75 mm and z_h was 117.39 mm. The *defocus* was at 90.63%. The experimental setup and results are shown in Fig. 4.21 & Fig. 4.22 respectively.

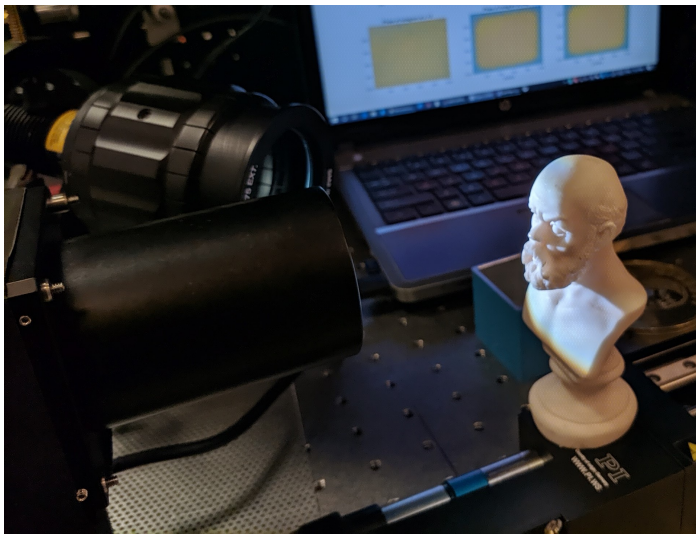

Figure 4.21: Apparatus setup for experiment 5 with the modified GP-SIDH system under reflective illumination.

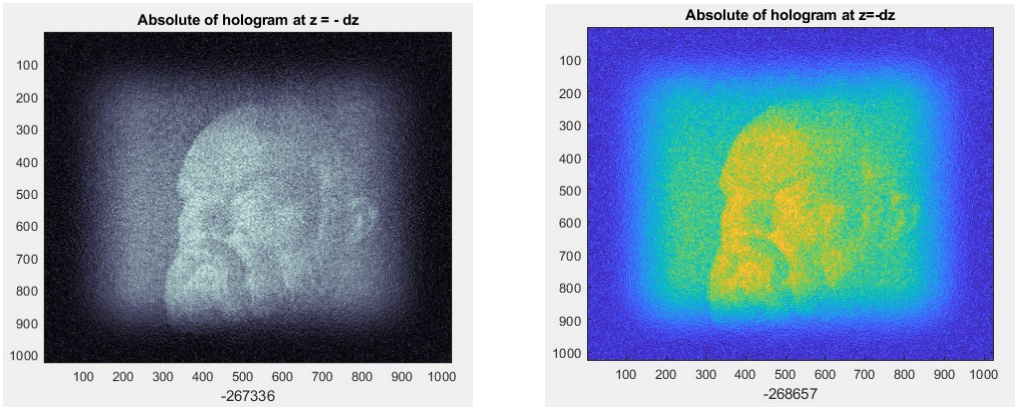

Figure 4.22: Reconstruction results for a Socrates figurine under reflective illumination with different colormaps.

4.2.2 Observations

The experiments conducted in the previous section is used to quantify various parameters for the modified GP-SIDH system architecture. Incoherent digital holograms were successfully recorded and the reconstruction process was carried out using the software MATLAB R2018 which consumes around 4.124 seconds for propagating the wavefields using the WD based modified Angular Spectrum propagation method as discussed in section 3.4.1. The *Defocus* test establishes a range of defocus where the reconstruction quality is optimum. For this system, 65% to 90% defocus from the perfectly focused rings configuration was suitable across all object distances for an overall good reconstruction. Objects placed under 200 mm are in the optimal FOV for the system apparatus provided the type of illumination is transmissive. After comparing different window functions based on a set of criterion, the Tukey window was selected as the best one in terms of reconstruction. The aperture size restricts the total amount of light entering through the system. Therefore, with increasing f-number, the pixel area diminishes. Finally, a 3D Socrates figurine is reconstructed under reflective illumination to demonstrate that the modified GP-SIDH system proposed is capable of hologram recording and simultaneous reconstruction at a given z plane under both transmissive and reflective illumination by incoherent light.

CHAPTER 5: CONCLUSION

To summarize, a modified GP-SIDH system is proposed which is a FINCH based incoherent holographic system. This system is capable of recording and simultaneously reconstructing the holograms by using a Wigner Distribution (WD) based AS propagation method. The system is configured with an convex objective lens, linear polarizer, a fluorescence bandpass filter, the GP lens, the 50 mm focal length Nikon lens used as a relay lens, and a polarized image sensor. The GP lens serves as a common-path polarization selective wavefront modulator. The parallel phase shifting method is achieved as a combination of the polarized image sensor, linear polarizer and the GP lens which enables recording of complex digital holograms and their simultaneous reconstruction. Quantifying the parameter defocus enables us to find the optimum defocus distance where we get the best reconstruction and the image quality is not degraded. The aperture size is directly related to the image reconstruction area of the holograms. The Tukey window, which is a tapered cosine window is applied to all the reconstructed result to eliminate the parasitic noise signals. The modified GP-SIDH system proposed here is highly cost-effective and simple to build. Further optimization to make the system more compact is an emerging area of research which explores innovative solutions to build a compact, portable size digital holographic system capable of real-time video recording.

REFERENCES

[1] K. Choi, J. Yim, and S.-W. Min, "Achromatic phase shifting self-interference incoherent digital holography using linear polarizer and geometric phase lens," *Optics express*, vol. 26, no. 13, pp. 16212–16225, 2018.

[2] K. Choi, K.-I. Joo, T.-H. Lee, H.-R. Kim, J. Yim, H. Do, and S.-W. Min, "Compact self-interference incoherent digital holographic camera system with real-time operation," *Optics express*, vol. 27, no. 4, pp. 4818–4833, 2019.

[3] D. Gabor, "A new microscopic principle," 1948.

[4] J. Rosen, A. Vijayakumar, M. Kumar, M. R. Rai, R. Kelner, Y. Kashter, A. Bulbul, and S. Mukherjee, "Recent advances in self-interference incoherent digital holography," *Advances in Optics and Photonics*, vol. 11, no. 1, pp. 1–66, 2019.

[5] A. W. Lohmann, "Wavefront reconstruction for incoherent objects," *JOSA*, vol. 55, no. 11, pp. 1555_1–1556, 1965.

[6] G. W. Stroke and R. C. Restrick III, "Holography with spatially noncoherent light," *Applied Physics Letters*, vol. 7, no. 9, pp. 229–231, 1965.

[7] J. Rosen and G. Brooker, "Digital spatially incoherent fresnel holography," *Optics letters*, vol. 32, no. 8, pp. 912–914, 2007.

[8] M. K. Kim, "Incoherent digital holographic adaptive optics," *Applied optics*, vol. 52, no. 1, pp. A117–A130, 2013.

[9] M. K. Kim, "Full color natural light holographic camera," *Optics Express*, vol. 21, no. 8, pp. 9636–9642, 2013.

[10] I. Yamaguchi and T. Zhang, "Phase-shifting digital holography," *Optics letters*, vol. 22, no. 16, pp. 1268–1270, 1997.

[11] B. W. Schilling, T.-C. Poon, G. Indebetouw, B. Storrie, K. Shinoda, Y. Suzuki, and M. H. Wu, "Three-dimensional holographic fluorescence microscopy," *Optics Letters*, vol. 22, no. 19, pp. 1506–1508, 1997.

[12] T.-C. Poon and G. Indebetouw, "Three-dimensional point spread functions of an optical heterodyne scanning image processor," *Applied optics*, vol. 42, no. 8, pp. 1485–1492, 2003.

[13] N. T. Shaked, B. Katz, and J. Rosen, "Review of three-dimensional holographic imaging by multiple-viewpoint-projection based methods," *Appl. Opt.*, vol. 48, no. 34, pp. H120–H136, 2009.

[14] Y. Rivenson, A. Stern, and J. Rosen, "Compressive multiple view projection incoherent holography," *Optics express*, vol. 19, no. 7, pp. 6109–6118, 2011.

[15] S. Pancharatnam, "Generalized theory of interference and its applications," in *Proceedings of the Indian Academy of Sciences-Section A*, vol. 44, pp. 398–417, Springer, 1956.

[16] M. V. Berry, "Quantal phase factors accompanying adiabatic changes," *Proceedings of the Royal Society of London. A. Mathematical and Physical Sciences*, vol. 392, no. 1802, pp. 45–57, 1984.

[17] K. Gao, H.-H. Cheng, A. K. Bhowmik, and P. J. Bos, "Thin-film pancharatnam lens with low f-number and high quality," *Optics express*, vol. 23, no. 20, pp. 26086–26094, 2015.

[18] N. V. Tabiryan, S. V. Serak, D. E. Roberts, D. M. Steeves, and B. R. Kimball, "Thin waveplate lenses of switchable focal length-new generation in optics," *Optics express*, vol. 23, no. 20, pp. 25783–25794, 2015.

[19] F. Shen and A. Wang, "Fast-fourier-transform based numerical integration method for the rayleigh-sommerfeld diffraction formula," *Applied optics*, vol. 45, no. 6, pp. 1102–1110, 2006.

[20] F. De Zela, "The pancharatnam-berry phase: Theoretical and experimental aspects," *Theoretical Concepts of Quantum Mechanics,(MR Pahlavani, ed.), InTech*, pp. 289–312, 2012.

[21] Sony, *Sony Polarization Image Sensor Technology*, 2018 (accessed March 20, 2019). `https://www.sony-semicon.co.jp/e/products/IS/polarization/technology.html`.

[22] FLIR, *FLIR Blackfly® S GigE polarized camera*, 2018 (accessed April 20, 2019). `https://www.flir.com/products/blackfly-s-gige/?model=BFS-PGE-51S5P-C`.

[23] R. K. Mantiuk, K. Myszkowski, and H.-P. Seidel, "High dynamic range imaging," *Wiley Encyclopedia of Electrical and Electronics Engineering*, pp. 1–42, 1999.

[24] J. Rosen, B. Katz, and G. Brooker, "Review of three-dimensional holographic imaging by fresnel incoherent correlation holograms," *3D Research*, vol. 1, no. 1, pp. 28–35, 2010.

[25] J. W. Goodman, *Introduction to Fourier optics*. Roberts and Company Publishers, 2005.

[26] G. Brooker, N. Siegel, J. Rosen, N. Hashimoto, M. Kurihara, and A. Tanabe, "In-line finch super resolution digital holographic fluorescence microscopy using a high efficiency transmission liquid crystal grin lens," *Optics letters*, vol. 38, no. 24, pp. 5264–5267, 2013.

[27] K. Choi, J. Yim, S. Yoo, and S.-W. Min, "Self-interference digital holography with a geometric-phase hologram lens," *Opt. Lett.*, vol. 42, pp. 3940–3943, Oct 2017.

[28] J. Hong and M. K. Kim, "Single-shot self-interference incoherent digital holography using off-axis configuration," *Optics letters*, vol. 38, no. 23, pp. 5196–5199, 2013.

[29] T. Tahara, T. Kanno, Y. Arai, and T. Ozawa, "Single-shot phase-shifting incoherent digital holography," *Journal of Optics*, vol. 19, no. 6, p. 065705, 2017.

[30] T.-C. Poon and J.-P. Liu, *Introduction to modern digital holography: with MATLAB*. Cambridge University Press, 2014.

[31] Y. Awatsuji, M. Sasada, and T. Kubota, "Parallel quasi-phase-shifting digital holography," *Applied physics letters*, vol. 85, no. 6, pp. 1069–1071, 2004.

[32] J. C. Wyant, "Interferometric optical metrology: basic principles and new systems," *Laser Focus*, vol. 18, no. 5, pp. 65–71, 1982.

[33] T. Kozacki, K. Falaggis, and M. Kujawinska, "Computation of diffracted fields for the case of high numerical aperture using the angular spectrum method," *Applied optics*, vol. 51, no. 29, pp. 7080–7088, 2012.

[34] N. Delen and B. Hooker, "Free-space beam propagation between arbitrarily oriented planes based on full diffraction theory: a fast fourier transform approach," *JOSA A*, vol. 15, no. 4, pp. 857–867, 1998.

[35] K. Matsushima and T. Shimobaba, "Band-limited angular spectrum method for numerical simulation of free-space propagation in far and near fields," *Optics express*, vol. 17, no. 22, pp. 19662–19673, 2009.

[36] T. Kozacki, "Numerical errors of diffraction computing using plane wave spectrum decomposition," *Optics Communications*, vol. 281, no. 17, pp. 4219–4223, 2008.

[37] D. Kirk *et al.*, "Nvidia cuda software and gpu parallel computing architecture," in *ISMM*, vol. 7, pp. 103–104, 2007.